ABSTRACT

SEARCH FOR CHARGED HIGGS BOSONS IN THE $\tau + \ell$ FINAL STATE WITH 36.1 fb^{-1} OF pp COLLISION DATA AT $\sqrt{s} = 13$ TeV WITH THE ATLAS EXPERIMENT

Elliot Wesley Parrish, Ph.D.
Department of Physics
Northern Illinois University, 2022
Dhiman Chakraborty and Jahred Adelman, Director

This dissertation uses 139 fb^{-1} of pp collision data collected at a center of mass energy of $\sqrt{s} = 13$ TeV by the ATLAS detector to search for charged Higgs bosons decaying to a tau lepton and a neutrino ($H^{\pm} \to \tau^{\pm}\nu_{\tau}$) in association with a leptonically decaying top quark. No significant excess was found, therefore limits are set at the 95% confidence level on the charged Higgs production cross section times the branching fraction into the $\tau^{\pm}\nu_{\tau}$ ranging from XX pb to XX fb. These limits are interpreted in the hMSSM benchmark scenario as an exclusion at 95% confidence on $\tan\beta$ as a function of $m_{H^{\pm}}$. In this scenario, for $\tan\beta = 60$, the $H^{\pm}$ mass range up to XXX GeV is excluded, with all values of $\tan\beta$ excluded for $m_{H^{\pm}} \leq XXX$ GeV.

NORTHERN ILLINOIS UNIVERSITY
DE KALB, ILLINOIS

DECEMBER 2022

SEARCH FOR CHARGED HIGGS BOSONS IN THE $\tau + \ell$ FINAL STATE WITH 36.1 fb^{-1} OF pp COLLISION DATA AT $\sqrt{s} = 13$ TeV WITH THE ATLAS EXPERIMENT

BY

ELLIOT WESLEY PARRISH

A DISSERTATION SUBMITTED TO THE GRADUATE SCHOOL

IN PARTIAL FULFILLMENT OF THE REQUIREMENTS

FOR THE DEGREE

DOCTOR OF PHILOSOPHY

DEPARTMENT OF PHYSICS

Dissertation Director:
Dhiman Chakraborty and Jahred Adelman

ACKNOWLEDGEMENTS

DEDICATION

To Dr. Dhiman Chakraborty. Thank you for everything.

TABLE OF CONTENTS

Page

List of Tables vii

List of Figures viii

Chapter

1 Introduction 1

2 Theory 2

2.1 The Standard Model 2

2.1.1 Particles 2

2.1.1.1 Fermions 3

2.1.1.2 Bosons 3

2.1.2 Interactions 5

2.1.2.1 Quantum Electrodynamics 5

2.1.2.2 ElectroWeak Interaction 6

2.1.2.3 Quantum Chromodynamics 7

2.1.3 The Higgs Mechanism 7

2.2 Supersymmetry 10

2.2.1 MSMM Particles 11

2.2.2 2 Higgs Doublet Model 12

2.3 Charged Higgs Bosons 12

2.3.1 Previous Result 13

Chapter Page

3 Experimental Apparatus 19
3.1 Particle Accelerators 19
3.1.1 Hadron Colliders. 19
3.1.2 The Large Hadron Collider 20
3.1.3 CERN Accelerator Complex 22
3.1.4 Luminosity. 24
3.2 The ATLAS Detector 26
3.2.1 Detector Coordinates 28
3.2.2 Magnet Systems 29
3.2.2.1 Solenoid System 30
3.2.2.2 Toroid System. 31
3.2.3 Inner Detector 31
3.2.3.1 Pixel 32
3.2.3.2 Semiconductor Tracker. 33
3.2.3.3 Transition Radiation Tracker 34
3.2.4 Calorimeters. 34
3.2.4.1 Liquid Argon Calorimeters. 36
3.2.4.2 Tile Calorimeter 37
3.2.5 Muon Spectrometer 39
3.2.6 Trigger System 40
4 Simulation 43
4.1 Event Generation and Hadronization 44
4.2 Detector Simulation 44

Chapter Page

5 Event Reconstruction . . . 46

5.1 Muon Identification . . . 46

5.2 e γ Identification . . . 46

5.3 Jet Clustering . . . 46

5.3.1 b-jet Tagging . . . 46

5.4 τ Identification . . . 46

5.5 $E_{\mathrm{T}}^{\mathrm{miss}}$ . . . 46

6 Search for Charged Higgs Bosons . . . 47

6.1 Signature and Event Selection . . . 47

6.1.1 Object Definitions . . . 47

6.1.2 Event Selections . . . 47

6.2 Datasets . . . 47

6.2.1 Signal Modeling . . . 47

6.3 Background Modeling . . . 47

6.4 Analysis Strategy . . . 47

6.4.1 Multivariate Analysis Techniques . . . 47

6.4.2 Training . . . 48

6.4.3 Feature Selection . . . 48

6.4.4 Hyperparameter Optimization . . . 48

6.5 Systematic Uncertainties . . . 48

6.6 Results . . . 48

7 Conclusion . . . 49

Appendices . . . 51

Appendix: TileCal Data Quality . . . 51

LIST OF TABLES

Table Page

2.1 Standard Model fermions and their properties [1] 4

2.2 Standard Model bosons and their properties [1] 4

2.3 Standard Model fermions and their ElectroWeak properties [1]. 6

2.4 SM particles and their MSSM partners [1] 11

2.5 2HDM extended Higgs sector [6] 12

3.1 LHC parameters [9] 21

3.2 Accelerator final energies 23

3.3 Design resolution of EM and hadronic calorimeters in the ATLAS Detector. . 35

LIST OF FIGURES

Figure Page

2.1 The Higgs potential defined in 2.2 with $\mu^2 < 0$ [4] 8

2.2 The distributions of the invariant mass of diphoton candidates after all selections for the combined 7 TeV and 8 TeV data sample. The inclusive sample is shown in (a) and a weighted version of the same sample in (c); the weights are explained in the text. The result of a fit to the data of the sum of a signal component fixed to $m_H = 126.5$ GeV and a background component described by a fourth-order Bernstein polynomial is superimposed. The residuals of the data and weighted data with respect to the respective fitted background component are displayed in (b) and (d). 14

2.3 Examples of leading-order Feynman diagrams contributing to the production of charged Higgs bosons in pp collisions: (a) non-resonant top-quark production, (b) single-resonant top-quark production that dominates at large $H^{\pm}$ masses, (c) double-resonant top-quark production that dominates at low $H^{\pm}$ masses. The interference between these three main diagrams becomes most relevant in the intermediate-mass region.. 15

2.4 Cross section of $H^{\pm}$ at various $\tan\beta$ values.. 15

2.5 Branching ratios of $H^{\pm}$ for (a) $\tan\beta = 10$ and (b) $\tan\beta = 50$ [7] 16

2.6 Limits on $\sigma(pp \to tbH^{\pm}xB(H^{\pm} \to \tau^{\pm}\nu))[pb]$. (a) is for the τ+jets subchannel (b) corresponds to the $\tau + \ell$ subchannel and (c) is the combination of the two subchannels. [8] 17

2.7 Limits on $\tan\beta$ as a function of $m_{H^{\pm}}$. [8] 18

3.1 Cross-section of cryodipole (lengths in mm). [10] 21

3.2 Field of the LHC dipole magnets. [11]. 22

3.3 The CERN accelerator complex. [12] 23

Figure Page

3.4 Cumulative luminosity versus time delivered to ATLAS (green), recorded by ATLAS (yellow), and certified to be good quality data (blue) during stable beams for pp collisions at 13 TeV center of mass energy in 2015-2018. The difference between the colored histograms reflects inefficiencies, especially those seen when restarting data taking. 25

3.5 The luminosity-weighted distribution of the mean number of interactions per bunch crossing for the 2015-2018 pp collision dataset at 13 TeV center of mass energy. 25

3.6 A display of a candidate Z boson event from proton-proton collisions recorded by ATLAS with LHC stable beams at a collision energy of 13 TeV. The Z boson candidate is reconstructed in a beam crossing with 28 additionally reconstructed primary vertices from the minimum bias interactions. The candidate event is reconstructed in the 2μ final state. In the left display, the red lines show the path of the two muons including the hits in the muon spectrometer and the yellow tracks are the remaining charged particles from the 29 vertices, with transverse momentum above 0.5 GeV. The colored squares in the lower display correspond to the position of the reconstructed vertices. The invariant mass of the two muons is 92.3 GeV. 26

3.7 Cut-away view of the ATLAS detector with major subdetectors highlighted. 27

3.8 Cross section view of the ATLAS detector with subdetectors labeled. Various types of particles radial trajectories are shown. 28

3.9 A diagram showing the pseudorapidity η and corresponding θ values. [13] . . 29

3.10 The ATLAS magnet systems. 30

3.11 (a) Cut-away view of the ATLAS Inner Detector. (b) Cross-sectional view of the ATLAS Inner Detector. 32

3.12 Interaction lengths as a function of η in the ATLAS calorimeters. The unlabeled brown color is the material in front of the EM calorimeters and the unlabeled cyan is the amount of material in front of the first active layer of the muon spectrometer. [20] 35

3.13 Cut-out view of the ATLAS detector's calorimeters. 36

3.14 A EMB module showing the accordion geometry and granularity. [20] 37

3.15 (a) Diagram of an individual TileCal module. (b) Azimuthal view of two TileCal modules with the IP being to the right. 38

Figure Page

3.16 Cut-out view of the ATLAS detector Muon Spectrometer. 40

3.17 The ATLAS TDAQ system in Run-2 showing the components relevant for triggering as well as the detector read-out and data flow. 42

4.1 A pictorial representation of the simulation chain used in the ATLAS experiment. [23]. 43

4.2 A pictorial representation of a parton shower of a ttH event. [23] 45

CHAPTER 1

INTRODUCTION

CHAPTER 2

THEORY

In this chapter, the theoretical motivation of a search for $H^{\pm} \rightarrow \tau^{\pm}\nu_{\tau}$ is described. Firstly, a review of the Standard Model of particle physics (SM) is laid out, then a brief overview of Supersymmetry focusing on the Minimal Supersymmetric Standard Model (MSSM). Finally, the Type II 2-Higgs Doublet Model's (2HDM) relation to the $H^{\pm}$ production cross section and subsequent branching ratio into SM particles is described as motivation for the choice of studying $H^{\pm} \rightarrow \tau^{\pm}\nu_{\tau}$.

2.1 The Standard Model

The SM of particle physics is a quantum field theory that describes all known matter and forces. The SM is built upon a gauge group of type $SU(3)_C \times SU(2)_L \times U(1)_Y$. The $SU(3)_C$ term dictates the strong interaction while the $SU(2)_L \times U(1)_Y$ term describes the electroweak interaction. These interactions occur between fundamental particles called fermions that comprise the known matter of the universe. The interactions, or forces, are mediated by fundamental particles called bosons.

2.1.1 Particles

The particles that make up the SM are separated into two groups according to their intrinsic angular momentum charge, or spin. Fermions are those that carry half-integer spin, and thus obey Fermi-Dirac statistics, while Bosons carry full integer spin values and obey Bose-Einstein statistics.

2.1.1.1 Fermions

The matter we encounter in everyday life is comprised of fermions. Fermions are subdivided into two groups, quarks and leptons. The quarks participate in the strong interaction via their color charge. Quarks cannot exist as a singular particle and thus combine into hadrons in a process called hadronization; the bound states they form are colorless. The proton and neutron are examples of hadrons. Leptons carry no color charge and therefore do not participate in strong force interactions. The fermions in the SM all participate in the electroweak interaction. However, the electromagnetic interaction is limited to those fermions that carry an electromagnetic charge. Section 2.1.2.2 describes the electroweak interaction in detail.

Fermions can then be further divided into three generations, each lepton has an electrically neutral weak force partner in the form of a neutrino. Table 2.1 lists all the SM fermions and their properties.

2.1.1.2 Bosons

Bosons are colloquially referred to as force-carriers in that the fundamental forces act via exchanging gauge bosons. This means that each force has an associated boson which is described by a field theory. The ElectroWeak quantum field theory (QFT) is more complicated, and is described in detail in section 2.1.2.2. Table 2.2 lists the SM bosons [1], their associated field theory and properties.

[1] excluding the Higgs

Table 2.1: Standard Model fermions and their properties [1]

	1^{st} Generation	2^{nd} Generation	3^{rd} Generation	Spin	EM Charge	Color	Mass
Quarks	Up (u)	Charm (c)	Top (t)	$\frac{1}{2}$	$+\frac{2}{3}$	✓	$m_u = 2.16^{+0.49}_{-0.26}$ MeV $m_c = 1.27 \pm 0.02$ GeV $m_t = 172.76 \pm 0.30$ GeV
	Down (d)	Strange (s)	Bottom (b)	$\frac{1}{2}$	$-\frac{1}{3}$	✓	$m_d = 4.67^{+0.48}_{-0.17}$ MeV $m_s = 93^{11}_{-5}$ MeV $m_b = 4.18^{0.03}_{-0.02}$ GeV
Leptons	Electron (e^-)	Muon (μ^-)	Tau (τ^-)	$\frac{1}{2}$	-1	X	$m_{e^-} = 0.51$ MeV $m_{\mu^-} = 105.65$ MeV $m_{\tau^-} = 1776.86 \pm 0.12$ MeV
	Electron Neutrino (ν_e)	Muon Neutrino (ν_μ)	Tau Neutrino (ν_τ)	$\frac{1}{2}$	0	X	$m_{\nu_e} < 1.1$ eV $m_{\nu_\mu} < 0.19$ MeV $m_{\nu_\tau} < 18.2$ MeV

Table 2.2: Standard Model bosons and their properties [1]

Field Theory	Boson	Spin	EM Charge	Color	Mass
Quantum Chromodynamics (QCD)	Gluon (g)	1	0	✓	0
Quantum Electrodynamics (QED)	Photon (γ)	1	0	X	$< 1\,\mathrm{x}\,10^{-18}$ eV
ElectroWeak Theory	$W^{\pm}$	1	± 1	X	80.379 ± 0.012 GeV
	Z^0	1	0	X	91.1876 ± 0.0021 GeV

2.1.2 Interactions

At its core, the SM relies upon symmetries. From these symmetries, conservation laws follow. It is these laws of conservation, and the breaking of tthe associated symmetry, that dictate the allowed interactions of matter. The first, being a symmetry under charge conjugation, mirror reflection, and time reversal is known as CPT symmetry. The symmetry between charge conjugation and mirror reflection (CP) can be broken in certain circumstances, but holds in strong and electromagnetic interactions. This breaking of CP symmetry occurs in the weak interaction and implies a non-symmetry between matter and antimatter. Since this symmetry holds for strong and electromagnetic interactions, baryon number ($B = \frac{1}{3}(n_q - n_{\bar{q}})$) and lepton number are conserved in SM interactions. Lepton generation number [2], electric charge, color charge, 4-momentum ($p = (E, \vec{p})$), and angular momentum are all conserved in the SM.

2.1.2.1 Quantum Electrodynamics

The electromagnetic force is governed by the QFT known as Quantum Electrodynamics (QED). This force is mediated by the photon, γ, a massless boson with EM charge 0. The EM force only affects, in other words, the photon only interacts with, charged particles; including all quarks and the e, μ, and τ leptons. Antiparticles are those that carry the opposite EM charge from their normal counterparts and differ in no other way. Antiparticles are denoted by a bar above the particle symbol ($e, \bar{e}$).

[2] Ignoring neutrino oscillations

2.1.2.2 ElectroWeak Interaction

The weak force is most often seen in nuclear decays and is mediated by the $W^{\pm}$ and Z^0 bosons. Due to the relatively large mass of these bosons, the weak force has a very limited range. The $W^{\pm}$ affects the third component of isospin (T_3), thus only coupling to so called left-handed fermions. This “handedness”, or chirality, is a property similar to color charge, in that an individual particle can have a number of different values. Table 2.3 contains the allowed values for isospin (T) and hypercharge (Y_W).

Table 2.3: Standard Model fermions and their ElectroWeak properties [1]

	1^{st} Generation	2^{nd} Generation	3^{rd} Generation	EM Charge	Y_W		T		T_3	
					LH	RH	LH	RH	LH	RH
Quarks	Up (u)	Charm (c)	Top (t)	$+\frac{2}{3}$	$+\frac{1}{3}$	$+\frac{4}{3}$	$\frac{1}{2}$	0	$\pm\frac{1}{2}$	0
	Down (d)	Strange (s)	Bottom (b)	$-\frac{1}{3}$	$+\frac{1}{3}$	$-\frac{2}{3}$	$\frac{1}{2}$	0	$\pm\frac{1}{2}$	0
Leptons	Electron (e^-)	Muon (μ^-)	Tau (τ^-)	-1	-1	0	$\frac{1}{2}$	0	$\pm\frac{1}{2}$	0
	Electron Neutrino (ν_e)	Muon Neutrino (ν_μ)	Tau Neutrino (ν_τ)	0	-1	-2	$\frac{1}{2}$	0	$\pm\frac{1}{2}$	0

The $W^{\pm}$ bosons have a T_3 component of isospin and act as raising or lowering operators on the T_3 component of left handed fermions. The Z does not have a T_3 component, and thus does not act on isospin of fermions. However, the Z boson instead transfers momentum, energy, and spin on all fermions irregardless of their chirality. At energies $>$ 100 GeV the electromagnetic and weak forces combine into the electroweak force. In fact, isospin and hypercharge combine to give electromagnetic charge. $Q_{EM} = T_3 + \frac{1}{2}Y_W$

2.1.2.3 Quantum Chromodynamics

Quantum chromodynamics (QCD) is the QFT that describes the strong force that holds together atomic nuclei and other objects called hadrons. The strong force interacts via the color charge [3] which can have values of either red, green, or blue. Particles that have a color charge cannot exist on their own, they must form colorless bound states called hadrons. Since the strong force grows with distance, if a quark is ejected out from a hadron, the stored energy is such that new particles with color charge will be spontaneously created from the vacuum, binding with the free quark in a process called hadronization. In a particle detector, the hadronization process cascades and creates showers of hadrons that are reconstructed as so called jets.

2.1.3 The Higgs Mechanism

The Higgs field is the mass generator of the SM and was first theorized by Peter Higgs [2], François Englert, and Robert Brout [3] in 1964. The SM itself has four massless Goldstone bosons that do not correspond to the observed bosons. Instead, the Higgs mechanism couples to them via a complex scalar doublet.

$$\phi = \begin{pmatrix} \phi^+ \\ \phi^0 \end{pmatrix} \tag{2.1}$$

The scalar potential that gives rise to this phenomena can be written as

$$V(\phi) = \mu^2 |\phi^\dagger \phi| + \lambda(|\phi^\dagger \phi|)^2 \tag{2.2}$$

[3]This color does is not the visual color we are used to. Merely a convenient analogous naming scheme.

When $\mu^2 > 0$ and $\lambda > 0$ the minimum of the potential $V(\phi)$ is 0. However, when $\mu^2 < 0$,

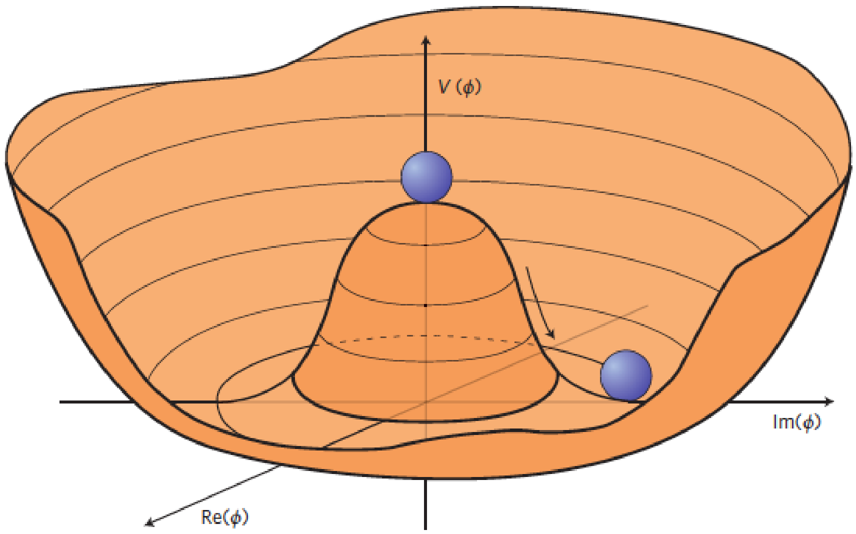

Figure 2.1: The Higgs potential defined in 2.2 with $\mu^2 < 0$ [4]

the scalar potential $V(\phi)$ takes the shape shown in figure 2.1 It follows that the vacuum expectation value (VEV) of ϕ is then

$$\langle\phi\rangle = \sqrt{\frac{-\mu^2}{2\lambda}} = \frac{\nu}{\sqrt{2}} \tag{2.3}$$

From here, convention states that we choose an arbitrary direction of the fluctuation as

$$\phi^0 = \frac{1}{\sqrt{2}}\binom{0}{\nu} \tag{2.4}$$

By choosing these values, $SU(2)$ and $U(1)_Y$ symmetries are broken, the Goldstone bosons are "eaten" and we are left with the remaining degree of freedom being the real scalar field $h(x)$

$$\phi(x) = \phi^0 + h(x) \tag{2.5}$$

Substituting in our definition of ϕ^0, we get

$$\phi = \frac{1}{\sqrt{2}}\begin{pmatrix} 0 \\ \nu + h(x) \end{pmatrix} \tag{2.6}$$

and couples to the gauge bosons via

$$(\frac{1}{2}g\vec{\sigma}\cdot\vec{W} + \frac{1}{2}g'B)\phi^0 \tag{2.7}$$

, where $\vec{\sigma}$ are the Pauli matrices, $\vec{W}$ are $W_{1,2,3}$, g is the weak coupling constant, and $g\prime$ is the hypercharge coupling constant. From this coupling, we get the four eigenstates that correspond to the observed bosons

$$\begin{aligned} W^{\pm} &= \frac{1}{\sqrt{2}}(W^1_\mu \mp iW^2_\mu) \\ Z^\mu &= \frac{-g\prime B_\mu + gW^3_\mu}{\sqrt{g^2 + g\prime^2}} \\ A^\mu &= \frac{gB_\mu + g\prime W^3_\mu}{\sqrt{g^2 + g\prime^2}} \end{aligned} \tag{2.8}$$

These eigenstates have corresponding mass values of

$$\begin{aligned} M_W^2 &= \frac{1}{4}g^2\nu^2 \\ M_Z^2 &= \frac{1}{4}(g^2 + g\prime^2)\nu \\ M_A^2 &= 0 \end{aligned} \tag{2.9}$$

The eigenstate labeled here as A is the photon. The Higgs boson was discovered in 2012 by the ATLAS and CMS collaborations at CERN with a mass of 125 GeV [5]. The scalar boson that was found appears to be the SM Higgs Boson.

2.2 Supersymmetry

While the SM is describes a wide range of physics to a high degree of accuracy, it is not without issues. To name a few, gravity, dark matter, and the observed matter-antimatter asymmetry of the universe are not defined by the SM. In addition, the SM defines the mass of neutrinos to be 0. However, because neutrino mixing is observed, where $\nu_e \rightarrow \nu_\mu$ is seen, neutrinos must have mass.

One promising model that offers solutions to many of these issues is Supersymmetry (SUSY). As discussed previously, the SM is built upon symmetries, and the breaking of these symmetries gives us electroweak unification. SUSY proposes another symmetry, this time between fermions and bosons.

$$\begin{aligned} Q|Fermion\rangle &= |Boson\rangle, \\ Q|Boson\rangle &= |Fermion\rangle \end{aligned} \tag{2.10}$$

Equation 2.10 shows how the SUSY operator Q acts on particles. SUSY naturally offers solutions to the “hierarchy problem” with the SM.

The hierarchy problem arises from the difference in electroweak ($M_W \sim 100$ GeV) and Planck ($M_P \sim 2.4\,\mathrm{x}\,10^{18}$ GeV) mass scales. For the Higgs mass to be on the scale of $M_H \sim 125$ GeV incredibly large and small mass terms must cancel perfectly, leading to a feeling of “unnaturalness”. SUSY brings many new particles into the picture, theorized to occupy the intermediate mass range leading to a more natural theory.

2.2.1 MSMM Particles

SUSY is a large group of theories, including many additional superpartner particles. The Minimal Supersymmetric Standard Model (MSSM) is the smallest extension of the SM that introduces SUSY. In the MSSM, each SM particle is part of a supermultiplet with it's superpartner where both particles have the same quantum numbers, except spin. If this supersymmetry is unbroken, then the superpartner and the SM particle would have the same mass as well. However, SUSY has not been observed, so the supersymmetry must be broken putting the mass scale on the TeV scale.

Table 2.4: SM particles and their MSSM partners [1]

Name	SM	MSSM
Spin-$\frac{1}{2}$ quarks and spin-0 squarks		
(s)up	u	$\tilde{u}$
(s)down	d	$\tilde{d}$
(s)charm	c	$\tilde{c}$
(s)strange	s	$\tilde{s}$
(s)top	t	$\tilde{t}$
(s)bottom	b	$\tilde{b}$
Spin-$\frac{1}{2}$ leptons and spin-0 sleptons		
(s)electron	e	$\tilde{e}$
(s)electron (s)neutrino	ν_e	$\widetilde{\nu_e}$
(s)muon	μ	$\tilde{\mu}$
(s)muon (s)neutrino	ν_μ	$\widetilde{\nu_\mu}$
(s)tau	τ	$\tilde{\tau}$
(s)tau (s)neutrino	ν_τ	$\widetilde{\nu_\tau}$
Spin-0 Higgs and spin-$\frac{1}{2}$ Higgsinos		
Higgs(ino)	H	$\tilde{H}$
gluon (gluino)	g	$\tilde{g}$
W (Wino)	$W^{\pm}$, W^0	$\widetilde{W^{\pm}}, \widetilde{W^0}$
B (Bino)	B^0	$\widetilde{B^0}$

Table 2.4 lists the MSSM supermultiplets and the associated naming conventions.

2.2.2 2 Higgs Doublet Model

Having only one Higgs chiral supermultiplet with hypercharge $Y_W = \pm\frac{1}{2}$ leads to a gauge anomaly. This can be resolved by introducing two Higgs doublets with hypercharge $Y_W = \frac{1}{2}$ and $Y_W = -\frac{1}{2}$. Such is the case with the MSSM which requires two complex doublet scalar fields where one couples to the up-type quarks and the other couples to down-type quarks and charged leptons. At this point, the MSSM has 8 degrees of freedom. Following the same type of symmetry breaking described in subsection 2.1.3 Three of these degrees of freedom give the observed $W^{\pm}$ and Z^0 bosons. This leaves us with the extended Higgs sector shown

Table 2.5: 2HDM extended Higgs sector [6]

light neutral scalar	h^0
heavy neutral scalar	H^0
neutral pseudoscalar	A^0
two charged scalars	$H^{\pm}$

in table 2.5, where the h^0 is the SM-like Higgs that was discovered by ATLAS and CMS in 2012. When referring to the charged Higgs bosons, we often refer to them using one symbol $H^{\pm}$. In the 2HDM we have two free parameters[4], the masses of the $H^{\pm}$ and the ratio of their vacuum expectation values which is defined as $\tan\beta$.

2.3 Charged Higgs Bosons

Since the $H^{\pm}$ couplings are proportional to the fermion masses, the main production modes at the LHC are through $t\bar{t}$ and Wt diagrams where the W is replaced by a $H^{\pm}$.

The production diagrams considered in this dissertation can be seen in figure 2.3. The cross section at various $\tan\beta$ values can be seen as a function of $m_{H^\pm}$ in figure 2.4. As $\tan\beta$ goes to smaller values the $H^\pm$ cross section become smaller and at very small values the top Yukawa couplings become non-perturbative, meaning they are highly unlikely to occur. In this dissertation the decay channel considered is $H^\pm \to \tau^\pm\nu_\tau$. As can be seen in figure 2.5, the $H^\pm \to \tau^\pm\nu_\tau$ decay channel is especially relevant at low $m_{H^\pm}$ and high $\tan\beta$. The search described in this dissertation consists of two sub-channels, τ+jets and $\tau + \ell$, where the associated top decays either hadronically or leptonically respectively.

2.3.1 Previous Result

To add context to this dissertation, it is important to reference the results of the previous iteration of the search discussed in this dissertation. The ATLAS collaboration published a paper in 2018 covering the data taking years of 2015 and 2016 [8], whereas this dissertation covers the full Run-2 (2015-2018) dataset. Figure 2.6 shows the limits on the cross section and figure 2.7 shows the limits on $\tan\beta$ as a function of $m_{H^\pm}$.

The previous iteration of this analysis used boosted decision trees (BDT) binned in $m_{H^\pm}$, giving them five separate classifiers to cover the mass range of $90 - 2000$ GeV. The mass bins can be seen as the blue dotted lines in Figure 2.6c. It is important to note the inclusion of the mass range $90 - 200$ GeV, as [8] was the first search to include this mass region below the top quark mass of 175 GeV.

[4]Only regarding the charged Higgs bosons

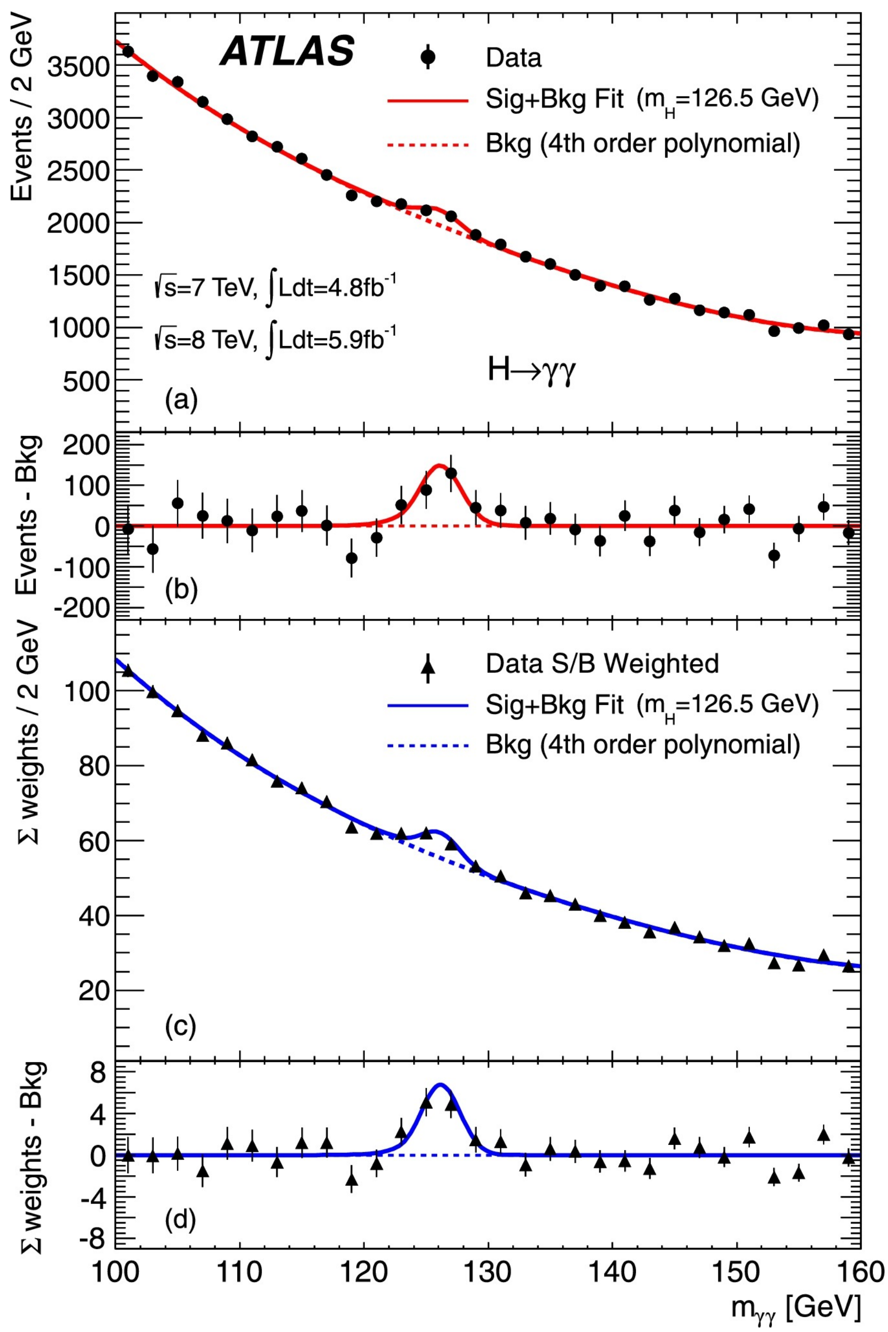

Figure 2.2: The distributions of the invariant mass of diphoton candidates after all selections for the combined 7 TeV and 8 TeV data sample. The inclusive sample is shown in (a) and a weighted version of the same sample in (c); the weights are explained in the text. The result of a fit to the data of the sum of a signal component fixed to $m_H = 126.5$ GeV and a background component described by a fourth-order Bernstein polynomial is superimposed. The residuals of the data and weighted data with respect to the respective fitted background component are displayed in (b) and (d).

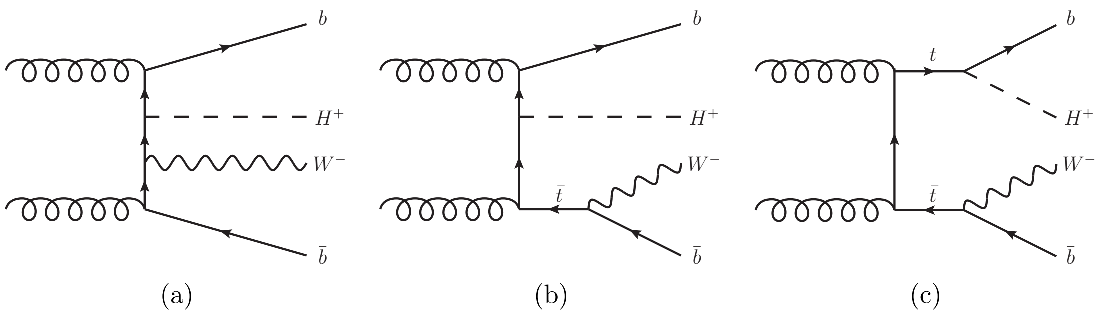

Figure 2.3: Examples of leading-order Feynman diagrams contributing to the production of charged Higgs bosons in *pp* collisions: (a) non-resonant top-quark production, (b) single-resonant top-quark production that dominates at large $H^{\pm}$ masses, (c) double-resonant top-quark production that dominates at low $H^{\pm}$ masses. The interference between these three main diagrams becomes most relevant in the intermediate-mass region.

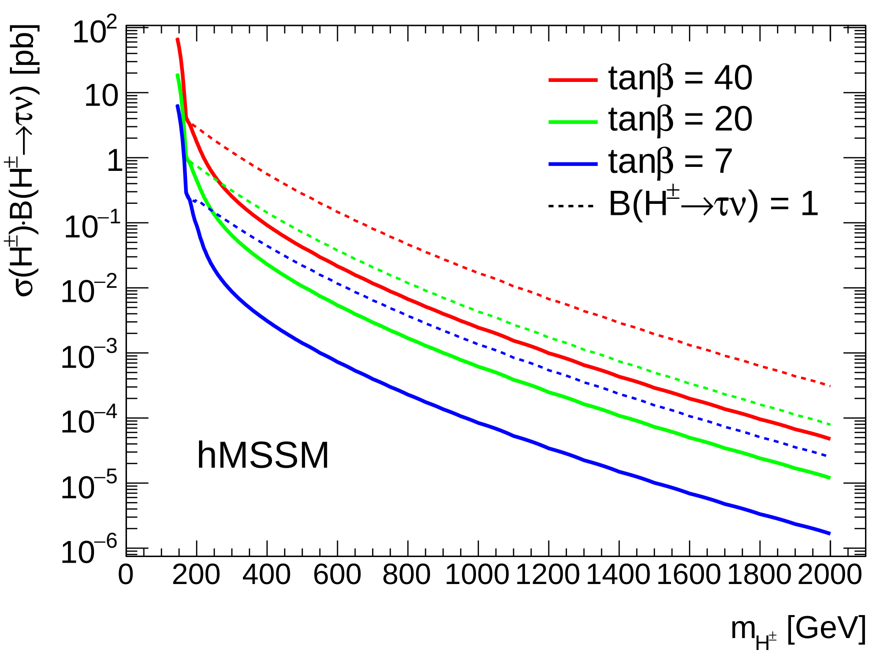

Figure 2.4: Cross section of $H^{\pm}$ at various $\tan\beta$ values.

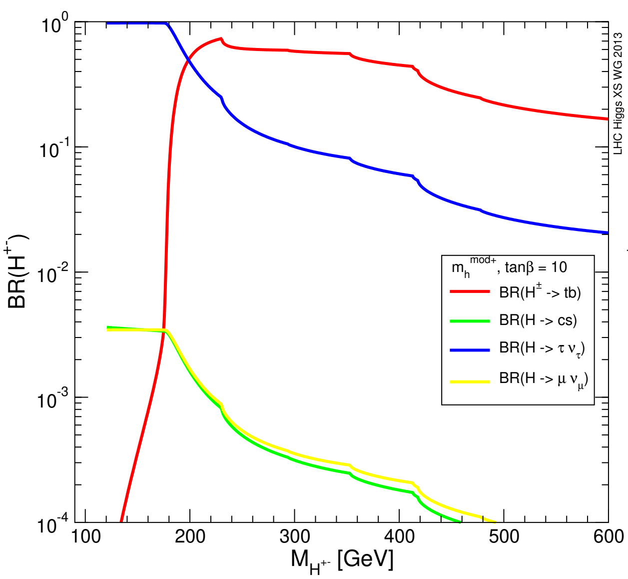

(a)

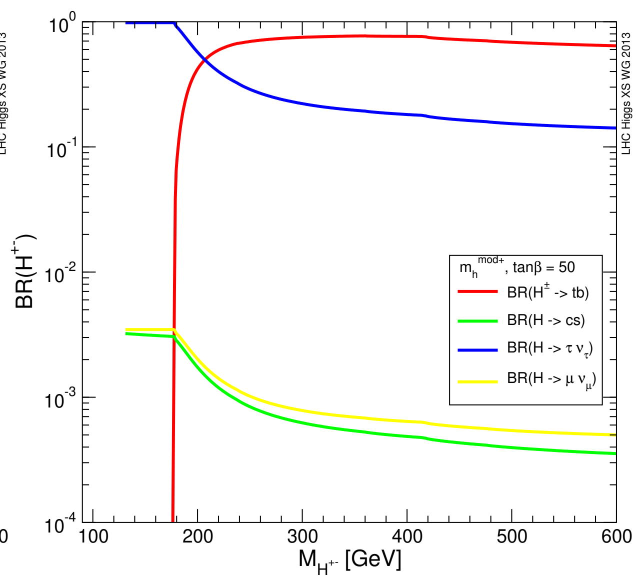

(b)

Figure 2.5: Branching ratios of $H^{\pm}$ for (a) $\tan\beta = 10$ and (b) $\tan\beta = 50$ [7]

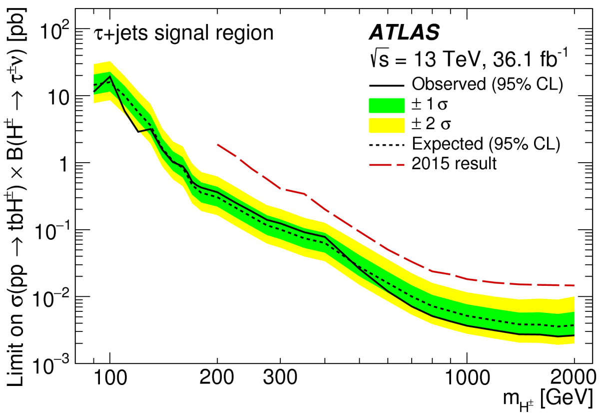

(a)

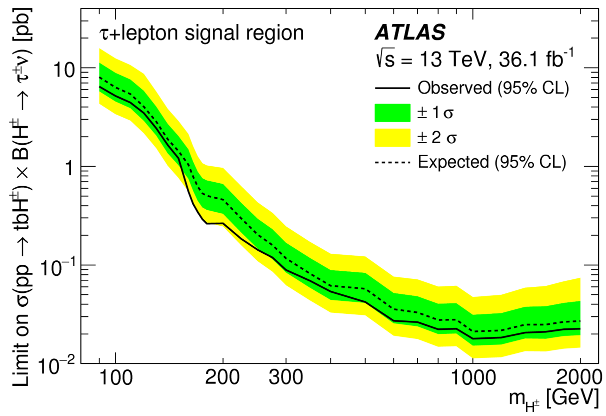

(b)

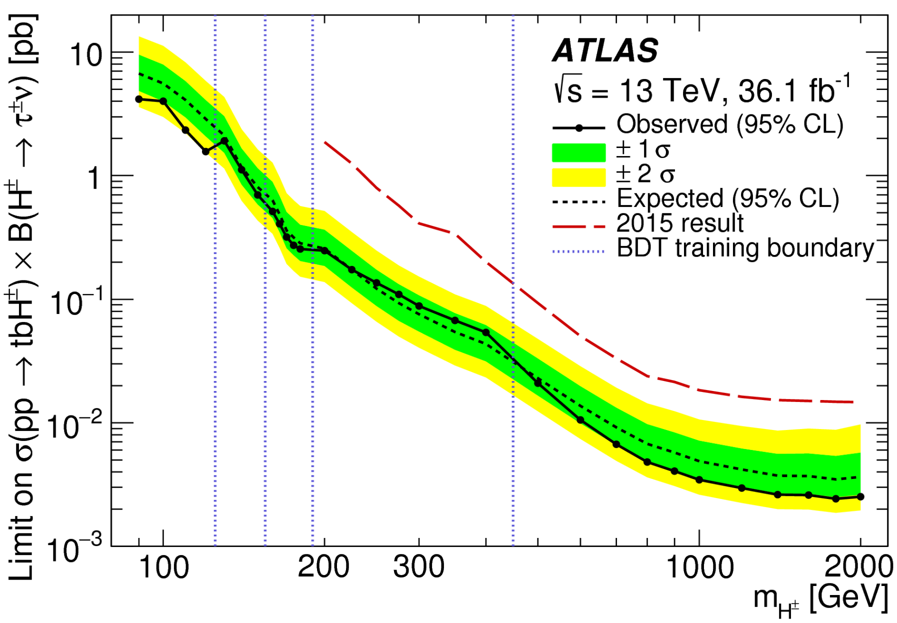

(c)

Figure 2.6: Limits on $\sigma(pp \to tbH^{\pm} x B(H^{\pm} \to \tau^{\pm}\nu))[pb]$. (a) is for the τ+jets subchannel (b) corresponds to the $\tau + \ell$ subchannel and (c) is the combination of the two subchannels. [8]

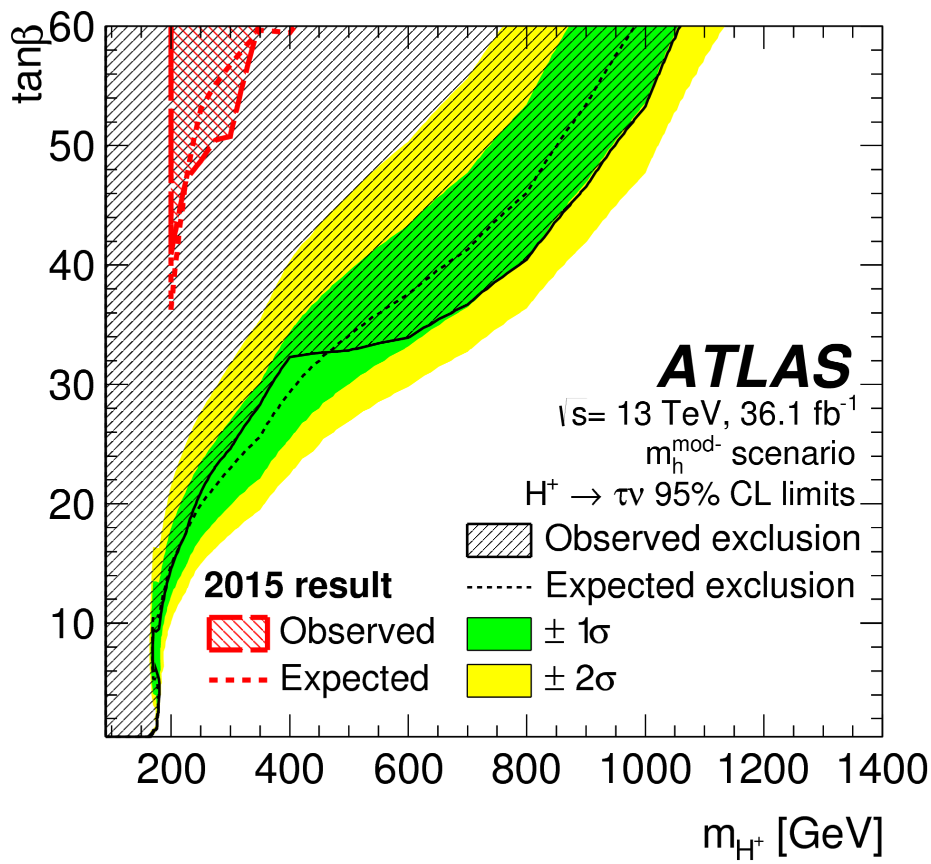

Figure 2.7: Limits on $\tan\beta$ as a function of $m_{H^\pm}$. [8]

CHAPTER 3

EXPERIMENTAL APPARATUS

3.1 Particle Accelerators

To study the Standard Model, the Higgs boson, and hints of new physics, particle accelerators are used. Particle accelerators can be categorized as either fixed target or colliders. As the naming suggest, in a fixed target accelerator the beam hits a target that then produces the desired particle collisions. Whereas a collider uses two opposite circulating beams that are then brought to collide inside a detector. A fixed target accelerator energy scales as $E_{CM} = \sqrt{E_{beam}}$ whereas a collider scales as $E_{CM} = 2\,E_{beam}$.

3.1.1 Hadron Colliders

There are two main types of particle colliders, those that use hadrons and those that use leptons. Lepton colliders are often referred to as precision machines, as the longitude momentum is known and backgrounds are well understood. The center of mass energy is well controlled in a lepton collider, meaning particles can be produced on resonance. On the other hand, due to the nature of hadrons not being fundamental particles a hadron collider produces a wide range of collisions. The constituents of a hadron participate in the collisions, meaning it is impossible to know the exact longitude momentum of the initial state. It is because of this exact reason that hadron colliders are referred to as discovery machines. The synchrotron radiation produced from a hadron collider is much lower than that of a lepton collider; meaning the beams are easier to control and can be pushed to higher energies without extra loses. The center of mass energy scales with $\frac{1}{m^4}$ in a hadron collider; again leading to an increased energy gain by simply using heavier particles.

3.1.2 The Large Hadron Collider

The Large Hadron Collider (LHC) is a 27 km circumference circular collider built outside of Geneva, Switzerland at CERN (Conseil Européen pour la Recherche Nucléaire). At center of mass energy 13.6 TeV, the LHC is the largest and highest energy particle accelerator ever built. There are four main collision points along the LHC: the ATLAS, CMS, ALICE, and LHCb experiments. ATLAS and CMS are general purpose particle detectors while ALICE and LHCb focus on heavy ion collisions. The numbers stated in the following sections are in reference to proton-proton collisions.

The LHC consists of 1104 NbTi superconducting dipole magnets, each being 15 m long, weighing 35 tonnes, cooled to 2 K, operating at 11,000 Amps, and produce a magnetic field of 8.3 T. A cross-section of a dipole magnet and the surrounding cryogenic system can be see in figure 3.1. The dipole magnets are used to bend the beam around the ring with another 128 used in the beam dump system to remove the beam safely from the LHC. A 2-in-1 configuration is used within the dipole magnets to create the required magnetic fields to bend two equally charged beams in opposite directions. A diagram of the magnetic fields in this configuration produced can be seen in 3.2. To focus the beam in the horizontal and vertical planes two quadrapole magnets are used; one magnet focuses in one plane while defocusing in the other. The end result is a horizontally and vertically focused beam. While in the LHC, the hadrons are accelerated using radiofrequency cavities. Table 3.1 lists some information on the LHC.

Table 3.1: LHC parameters [9]

Circumference	26,659 m
Dipole operating temperature	1.9 K
Dipole magnets	1232
Quadrapole magnets	392
Radiofrequency cavities	16 (8 per beam)
Beam energy	6.5 TeV (13 CoM TeV)
Protons per bunch	1.2x10^{1}1
Bunches per beam	2808
Revolutions per second	11245
Collisions per second	1,000,000,000

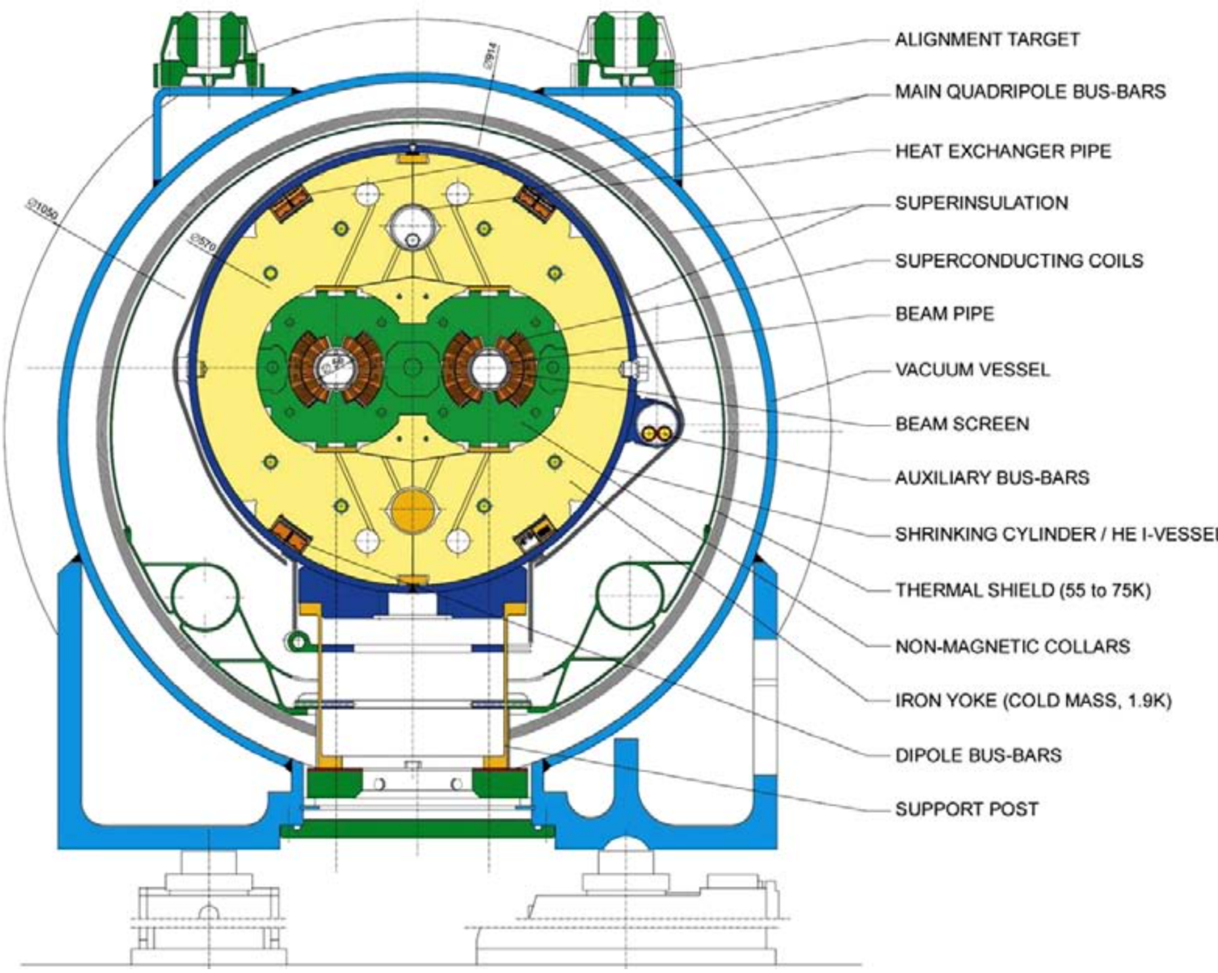

Figure 3.1: Cross-section of cryodipole (lengths in mm). [10]

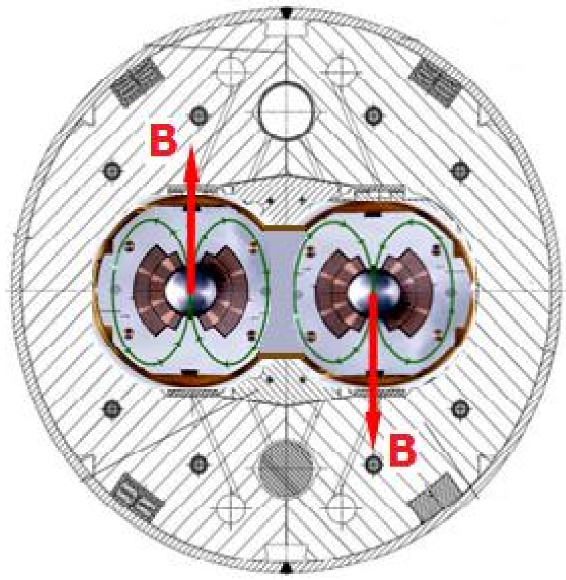

Figure 3.2: Field of the LHC dipole magnets. [11]

3.1.3 CERN Accelerator Complex

There are a series of accelerators used to get each beam up to its final energy of 6.5 TeV. The protons used in collisions are sourced from hydrogen atoms. The hydrogen is ionized, leaving the nucleus consisting of one proton, these protons are then accelerated in radiofrequency (RF) cavities. Figure 3.3 shows in detail the full accelerator complex at CERN.[1] The protons used in the LHC start the accelerating process in the linear accelerator LINAC 2. They then are accelerated in the booster, PS, SPS, and are finally injected at the LHC where they are accelerated to the final 6.5 TeV beam energy. The final energies of protons from each accelerator can be seen in Table 3.2.

[1]Figure 3.3 shows the newer LINAC 4 at the start of Run-3. This work is concerning data taken with LINAC 2.

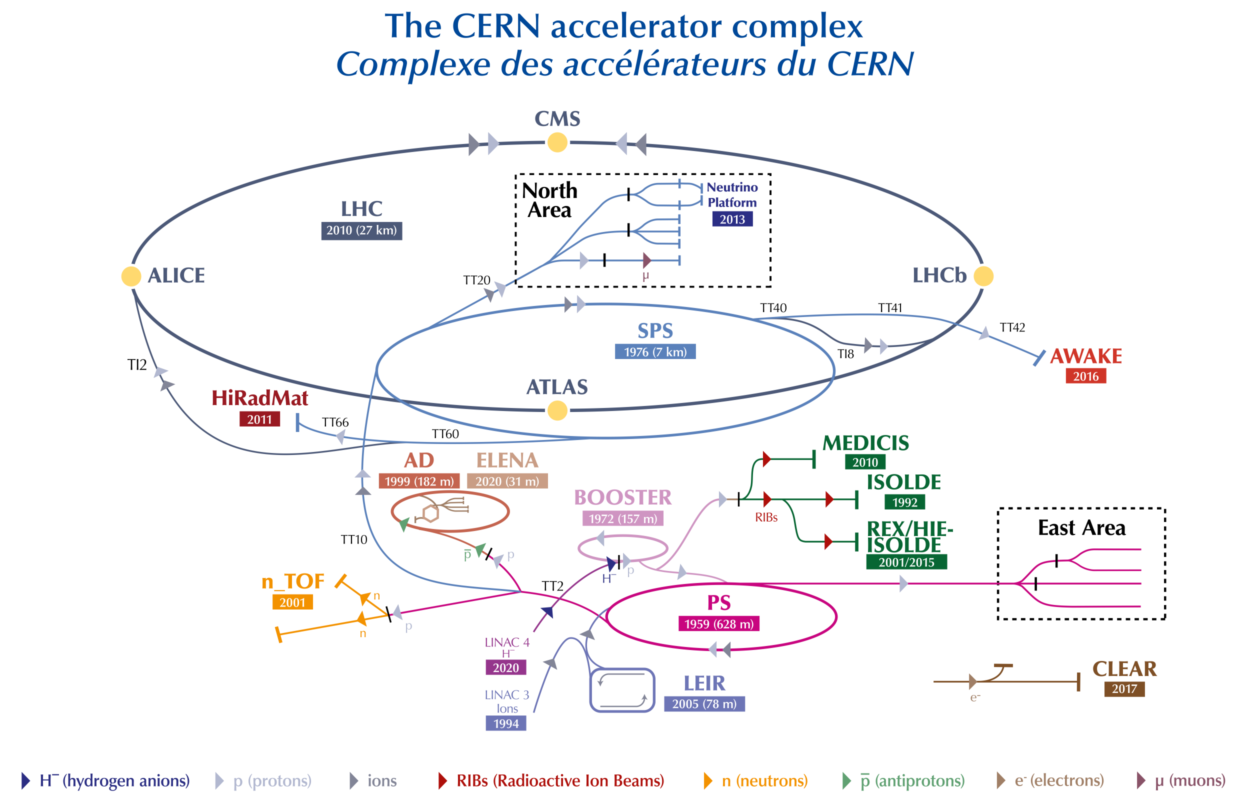

[redacted]

Figure 3.3: The CERN accelerator complex. [12]

Table 3.2: Accelerator final energies

Accelerator	Final Energy
LINAC 2	50 MeV
Booster	1.4 GeV
Proton Synchrotron (PS)	26 GeV
Super Proton Synchrotron (SPS)	450 GeV
Large Hadron Collider (LHC)	6.5 TeV

3.1.4 Luminosity

The amount of data collected from colliders is often referred to in terms of luminosity. Luminosity is measured in terms of inverse barns, where $1\,b = 10^{-28}\,m^2$. Instantaneous luminosity of one bunch crossing can be written as

$$\mathcal{L}_{bunch} = \frac{\mu f}{\sigma} \tag{3.1}$$

where σ is the cross section and can be thought of as the probability of a collision occurring, μ is the number of inelastic interactions per bunch crossing, and f is the revolution frequency of the LHC $f = 11246$ Hz. Therefore, the total instantaneous luminosity is

$$\mathcal{L} = N_b \frac{\langle \mu \rangle f}{\sigma} \tag{3.2}$$

where $\langle \mu \rangle$ is the average number of inelastic interactions per bunch crossing.

The integrated luminosity then corresponds to the total amount of data that was taken during a time period and can be seen for the LHC Run-2 in 3.4 The value of $\langle \mu \rangle$ changed throughout data taking and can be seen in Figure 3.5 and is referred to as pileup because the higher the $\langle \mu \rangle$ value, the more messy a collision becomes. The effect of high pileup can be seen in Figure 3.6, a collision event taken in 2018 with 29 reconstructed vertices shown on the bottom right as colored circles.

A common calculation using the total integrated luminosity is shown in Equation 3.3; where the number of times a particular process was produced is calculated.

$$N_x = \mathcal{L}\sigma_x \tag{3.3}$$

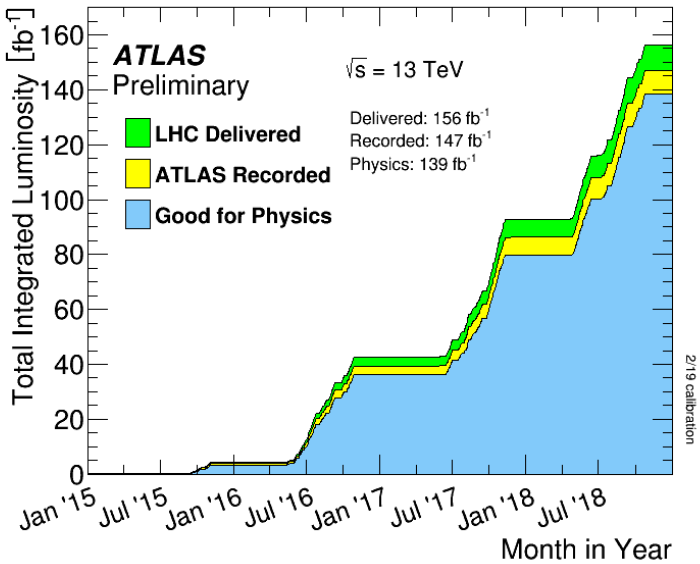

Figure 3.4: Cumulative luminosity versus time delivered to ATLAS (green), recorded by ATLAS (yellow), and certified to be good quality data (blue) during stable beams for pp collisions at 13 TeV center of mass energy in 2015-2018. The difference between the colored histograms reflects inefficiencies, especially those seen when restarting data taking.

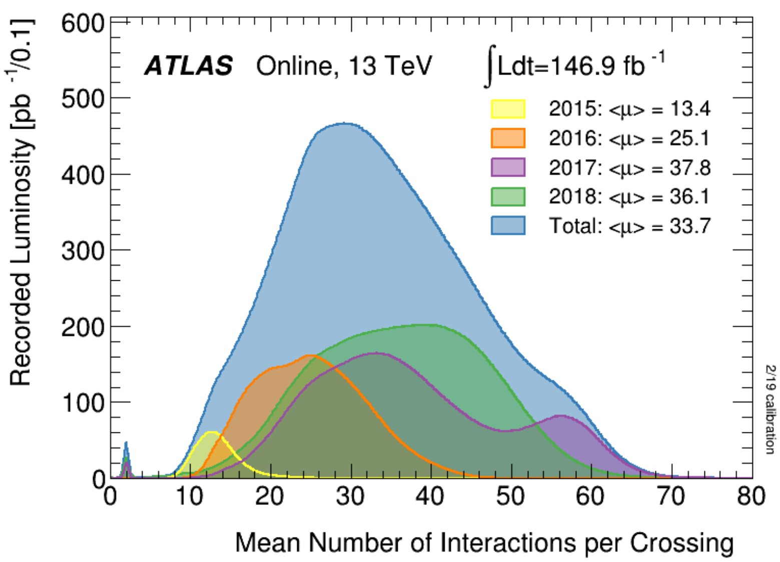

Figure 3.5: The luminosity-weighted distribution of the mean number of interactions per bunch crossing for the 2015-2018 pp collision dataset at 13 TeV center of mass energy.

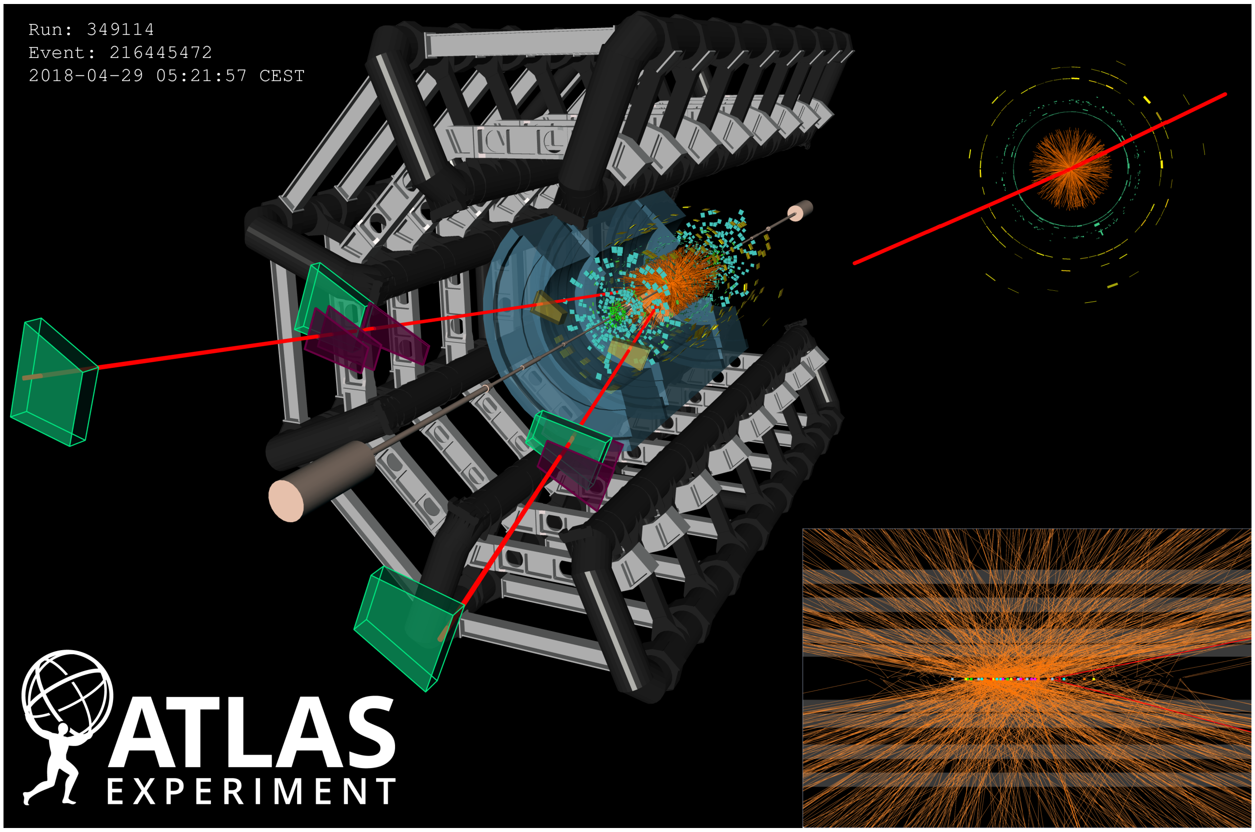

Figure 3.6: A display of a candidate Z boson event from proton-proton collisions recorded by ATLAS with LHC stable beams at a collision energy of 13 TeV. The Z boson candidate is reconstructed in a beam crossing with 28 additionally reconstructed primary vertices from the minimum bias interactions. The candidate event is reconstructed in the 2μ final state. In the left display, the red lines show the path of the two muons including the hits in the muon spectrometer and the yellow tracks are the remaining charged particles from the 29 vertices, with transverse momentum above 0.5 GeV. The colored squares in the lower display correspond to the position of the reconstructed vertices. The invariant mass of the two muons is 92.3 GeV.

where again, σ is the cross section. In this case, the cross section corresponding to process x.

3.2 The ATLAS Detector

The ATLAS (**A** **T**oroidal LHC **A**pparatu**S**) detector is one of two general purpose particle detectors on the LHC. The other being the **C**ompact **M**uon **S**olenoid (CMS). ATLAS, like other particle detectors, is comprised of four main components; the inner detector, calorimeters, muon system, and the magnet system. Each component has several types of technology in order to measure the energy of all possible particle decays.[2] The full ATLAS detector measures 44 m in length, 25 m in diameter, and weighs over 7000 tonnes. Figure 3.7 shows a 3D model of the ATLAS detector and Figure 3.8 shows a cross section of the detector and various particles trajectory.[3] All of the subdetectors output data to the Trigger and Data Acquisition (TDAQ) system that selects collisions with interesting physics using a complex mix of hardware and software algorithms detailed in 3.2.6.

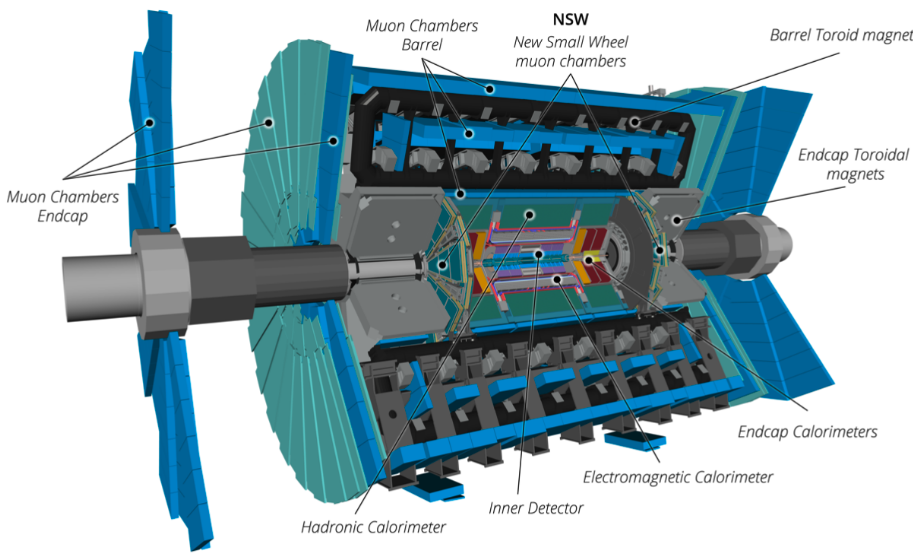

Figure 3.7: Cut-away view of the ATLAS detector with major subdetectors highlighted.

[2]Neutrinos are not directly detected, but inferred via a missing transverse energy calculation described in Section 5.5.

[3]Figure 3.7 shows the New Small Wheel muon-chambers. This dissertation concerns data collected with the old Small Wheel muon-chambers.

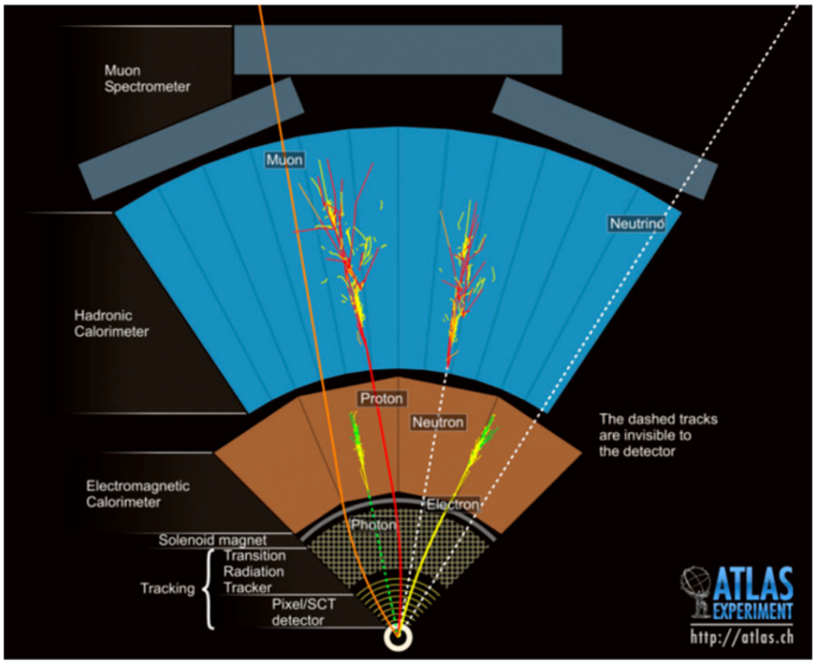

Figure 3.8: Cross section view of the ATLAS detector with subdetectors labeled. Various types of particles radial trajectories are shown.

3.2.1 Detector Coordinates

Since ATLAS is a cylinder, it is convenient to start with polar cylindrical coordinates. For ATLAS, the z-axis is inline with the beam line, the x-axis points towards the center of the LHC ring, and the y-axis points vertically. However, since particle collisions are relativistic by nature, a set of Lorentz invariant coordinates is much more useful. The radial coordinate r defines the radial distance from the interaction point (IP) at the center of ATLAS, ϕ is the azimuthal angle describing the angle from the x-axis in, and η, the pseudorapidity, is defined as

$$\eta \equiv -ln(tan(\frac{\theta}{2})) \tag{3.4}$$

where θ is the angle from the y-axis. It is in the differences in η between particles that provides the Lorentz invariance in this coordinate system of (r, ϕ, η). Due to the large collision energies of the LHC, the pseudorapidity is a close estimate to the true rapidity of the particles.

$$y \equiv \frac{1}{2} ln(\frac{E + p_Z}{E - p_Z}) \approx \eta \tag{3.5}$$

When speaking of differences in particle locations within ATLAS, ΔR is often used.

$$\Delta R \equiv \sqrt{(\Delta\eta)^2 + (\Delta\phi)^2} \tag{3.6}$$

Figure 3.9 shows visually how η relates to θ. In the ATLAS detector, the central barrel section corresponds to a range of $|\eta| < 1$.

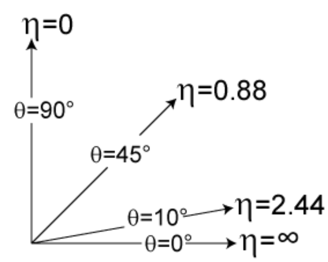

Figure 3.9: A diagram showing the pseudorapidity η and corresponding θ values. [13]

3.2.2 Magnet Systems

The ATLAS detector makes use of two superconducting magnet systems; a central solenoid and a toroid system. Both systems provide large magnetic fields to curve charged particles. The curvature can be used to measure the electromagnetic charge and charge to mass ratio, effectively measuring the momentum of charged particles. Figure 3.10 shows the magnets in ATLAS.

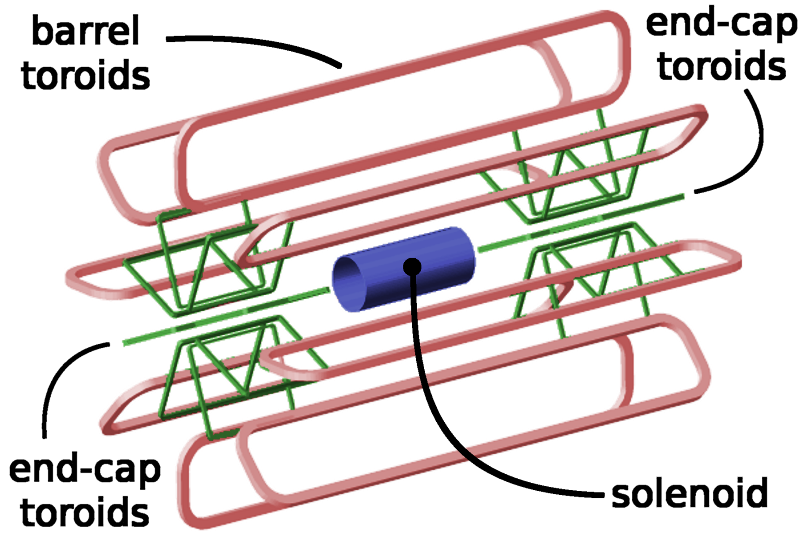

Figure 3.10: The ATLAS magnet systems.

3.2.2.1 Solenoid System

The central solenoid encases the Inner Detector (ID), creating an axially symmetric 2 T magnetic field. This magnetic field bends charged particles in the transverse plane throughout the ID. The solenoid magnet itself measures 5.3 m in length and 2.63 m in diameter. In an effort to decrease the amount of material in front of the calorimeters the solenoid magnet was made to be thin. It is a single-layer coil with approximately 1200 turns of NbTi superconducting wires encased in Al-Cu to structurally stabilize the magnet material [14]. The steel structure within the Tile calorimeter acts as the magnetic flux return for the solenoid magnet system. 70% of this flux passes through the supporting girder structure, 25% through the active calorimeter material, and roughly 2% through the front-plates of the Tile calorimeter [15].

3.2.2.2 Toroid System

The ATLAS detector gets its name from the toroid magnetic system that is critical in the identification of high energy muons. The toroid system bends any charged particles that make it past the calorimeters along the beam axis. This is achieved through a radially symmetric magnetic field of 3.9 T in the barrel and 4.1 in the end-caps. The barrel toroid system is comprised of 8 air core superconducting toroid magnets that each measure 25 m in length, 10 m in diameter, and weigh 750 tonnes. The superconducting wires are the same used in the solenoid, NbTi encased in Al-Cu [16]. Each magnet is encased in a stainless steel cryogenic chamber, or cryostat. The toroid magnet system has two end-cap toroids that are very similar in construction to the barrel toroids. The end-cap toroids also have 8 coils measuring 5 m in length and 10 m in diameter. Instead of individual cryostats for each coil, the end-caps are encased in large cryostats that hold all 8 coils. This allows the end-caps to be pulled out and offers easy access to the rest of the detector. Just like with the central solenoid system, the design of the toroid system was chosen to limit the amount of material between detector components. A solenoid magnet of similar size to the toroid system would not only add more material, but would be cost prohibitive as well.

3.2.3 Inner Detector

The ID is the inner-most detector, closest to the IP and is used to track the trajectory of charged particles leading to the measurement of electromagnetic charge and momentum. The ID is immersed in the 2 T magnetic field provided by the central solenoid described in section 3.2.2.1 and covers a pseudorapidity range of $|\eta| < 2.5$. The three subdetectors within the ID can be seen in Figure 3.11, the Pixel, **S**emi**C**onductor **T**racker (SCT), and the **T**ransition

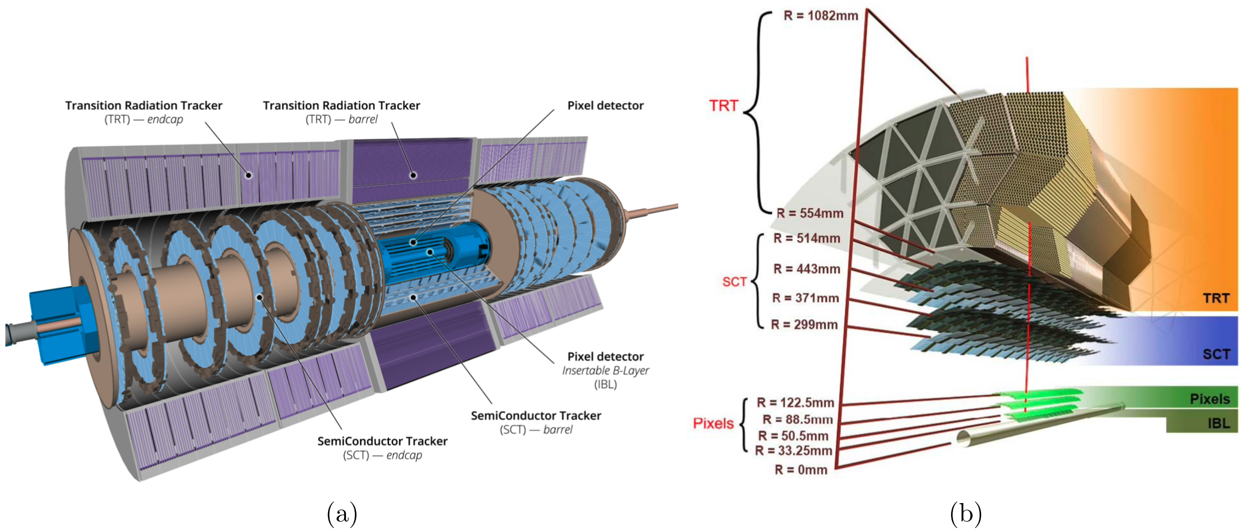

Figure 3.11: (a) Cut-away view of the ATLAS Inner Detector. (b) Cross-sectional view of the ATLAS Inner Detector.

Radiation **T**racker (TRT). Like the toroid system, and many of the other subdetectors, the ID is comprised of barrel and end-cap segments. The ID barrel section is 1.6 m in length and covers $|\eta| < 1$ while the end-caps measure over 7 m in length and cover $1 < |\eta| < 2.5$.

A track is considered good if there are hits in at least 3 pixel layers and 8 strips. The ID tracking system was designed with a resolution of

$$\frac{\sigma_{p_\mathrm{T}}}{p_\mathrm{T}} = 0.05\%\, p_\mathrm{T} \oplus 1\% \tag{3.7}$$

3.2.3.1 Pixel

The detector closest to the beam and IP is the Pixel Detector. The Pixel Detector is designed to measure with high-precision and high-granularity. The barrel Pixel detector consists of three layers of n-type silicon substrate with n-type implants. The closest layer to the IP sits at 50.5 mm and the outermost layer extends out to 12 cm. This combination gives the Pixel Detector the ability to determine the impact parameters of collisions with incredible precision. Due to the high radiation dose this close to the IP, the Pixel Detector was designed to be operated only in partial depletion. Each pixel cell measures $200\mu m \times 400\mu m \times 250\mu m$. There are five Pixel disks on each end-cap of the ID. In total there are 1,744 modules, 46,080 readout channels per module, giving over 80 million channels with a spatial resolution of $10\,\mu m(R-\phi) \times 115\,\mu m(z)$ [17].

In order to keep up with the increased demand of Run-2 data taking conditions, an additional layer of pixels was installed in the Long Shutdown 1 (LS1) between 2013 and 2015. This **I**nsertable **B** **L**ayer (IBL) provides even finer granularity tracking with pixel cells measuring $50\,\mu m \times 250\,\mu m$ installed at a radial distance of $R = 33.25$ mm from the IP and a spatial resolution of $8\,\mu m(R-\phi) \times 40\,\mu m(z)$ [18]. The IBL has proved incredibly useful in the reconstruction of displaced vertices from processes like b-jet hadronization and $\gamma \rightarrow e^+e^-$.

3.2.3.2 Semiconductor Tracker

Moving radially outward, the next subdetector is the SCT that provides tracking in the intermediate radial range from the IP and covers a range of $|\eta| < 2.5$. Similar to the Pixel Detector, the SCT has 4 barrel layers and 9 end-cap wheels on each side. The SCT provides four measurements per track via silicon microstrip detectors. Each microstrip is made of two $6.36 \times 6.40\,cm^2$ detectors glued end to end so each microstrip is $12.8\,cm$ long. Two microstrips are then glued back to back with a $40\,\mu rad$ angle. In total there are 768 strips, giving 6.2 million readout channels. The SCT has a spatial resolution of $17\,\mu m(R-\phi) \times 580\,\mu m(z)$ and can distinguish tracks with as small as a $200\,\mu m$ separation [19].

3.2.3.3 Transition Radiation Tracker

The final subdetector of the ID is the TRT ($R = 554\,\mathrm{mm} - 1082\,\mathrm{mm}$) . Instead of silicon detectors the TRT uses 4 mm diameter straw tubes; a hollow tube with a sense wire held at high voltage in the middle. The max length of a straw is 150 cm. The straws are filled with a gaseous mixture of $70\%\,\mathrm{Xe}, 27\%\,\mathrm{CO_2}$, $3\%\,\mathrm{O_2}$.[4] Charged particles ionize the gas mixture, thereby releasing an electron and an ion. The ion drifts to the straw surface and the electron drifts to the wire; this charge drift is then measured as a signal. The TRT checks the signals against two thresholds, a lower threshold for measuring the drift time to derive a position and a higher threshold that is used to identify transition radiation X-rays. The higher threshold provides discriminating power between charged pions and electrons.

The TRT consists of a barrel section and 18 wheels in each end-cap. In the barrel, there are 50,000 straws divided in two at the center to allow for two separate readouts. The end-caps have 320,000 straws. In total, there are 420,000 readout channels. Each straw provides a spatial resolution of $170\mu m$. [19]

3.2.4 Calorimeters

The ATLAS detector makes use of two types of sampling calorimeters, one that uses liquid argon as the active medium and another that uses scintillating plastic tiles. Both types of calorimeters are designed to fully absorb particles via showering. Incoming particles interact with an absorber material and generate secondary particles. Those secondary particles interact with the absorber and create another set of particles. This cascading effect creates showers of particles inside the calorimeters. The shape and depth of these particles is important in the

[4] During Run-2 the Xe was replaced with Ar as a cost saving measure. Ar provides similar performance as Xe in tracking, but is less efficient in absorbing X-rays from transition radiation.

design choices for the calorimeters as well as particle identification. Two helpful variables when talking about shower depth are radiation length χ_0 and nuclear interaction length λ. χ_0 is defined as the distance where a particle has lost energy via bremsstrahlung equal to $\frac{1}{e}$.[5] Whereas λ is the mean free path of a hadron before undergoing a inelastic nuclear interaction. In order to fully absorb a wide energy range of incident particles the calorimeters are such that any path through them is at least $25\,\chi_0$ or $10\,\lambda$. Figure 3.12 shows the calorimeters and their nuclear interaction lengths as a function of η.

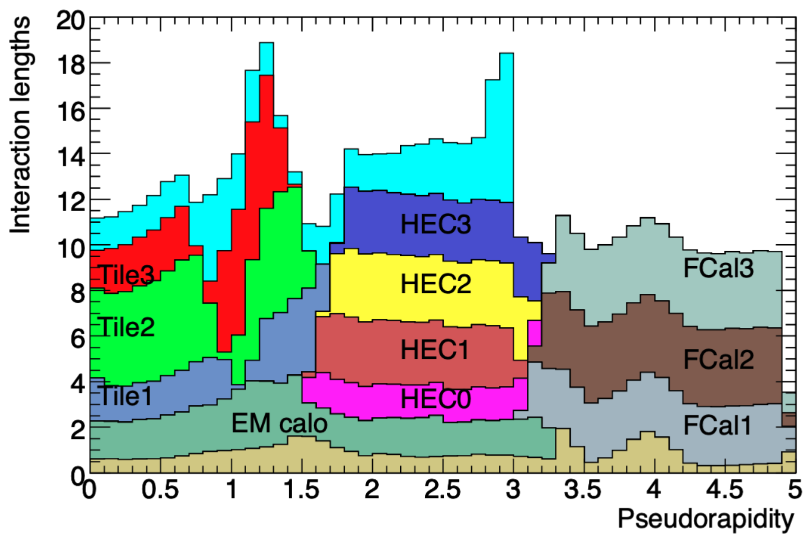

Figure 3.12: Interaction lengths as a function of η in the ATLAS calorimeters. The unlabeled brown color is the material in front of the EM calorimeters and the unlabeled cyan is the amount of material in front of the first active layer of the muon spectrometer. [20]

The design resolution of the calorimeters can be seen in Table 3.3.

Table 3.3: Design resolution of EM and hadronic calorimeters in the ATLAS Detector.

Calorimeter	Pseudorapidity range	Resolution
Electromagnetic	$\|\eta\| < 3.2$	$\frac{\sigma}{E} = \frac{10\%}{\sqrt{E}} \oplus 0.7\%$
Hadronic	$\|\eta\| < 3.2$	$\frac{\sigma}{E} = \frac{50\%}{\sqrt{E}} \oplus 3\%$
	$3.1 < \|\eta\| < 4.9$	$\frac{\sigma}{E} = \frac{100\%}{\sqrt{E}} \oplus 10\%$

The layout of calorimeters in the ATLAS detector can be seen in Figure 3.13.

[5] χ_0 can also be defined as $\frac{7}{9}$ of the mean free path of a high energy photon.

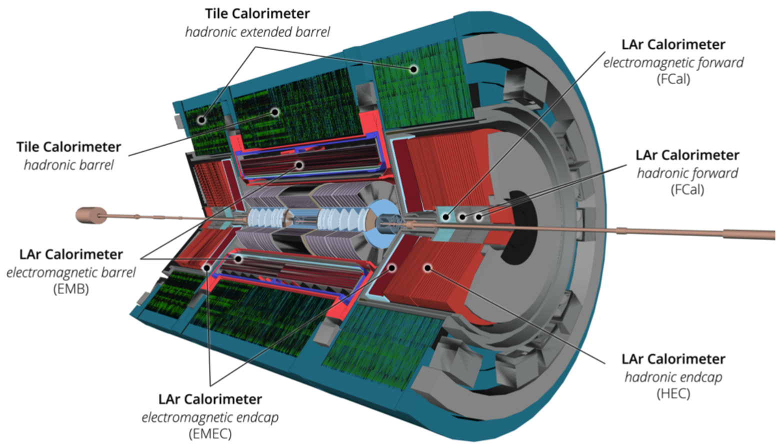

Figure 3.13: Cut-out view of the ATLAS detector's calorimeters.

3.2.4.1 Liquid Argon Calorimeters

A liquid argon (LAr) is based on a similar principle to the straw tubes of the TRT described in section 3.2.3.3. In this case, the LAr is the active medium that is ionized by the incoming particle. The free electron then drifts to an electrode, copper-tungsten in the case of the barrel LAr calorimeter. The drifting electrons are then readout as an electrical signal; there are approximately 180,000 LAr readout channels in the ATLAS detector. LAr was chosen as the active medium due to it's intrinsic radiation hardness, stability over time, and linear response. The LAr must be kept at very cold temperatures, around 85 K. To achieve this, the LAr calorimeters are kept in cryostats, the barrel calorimeter shares the cryostat and vacuum with the central solenoid.

There are four LAr calorimeters within the ATLAS detector. The main barrel section (EMB) is designed for electromagnetic calorimetry with a lead-stainless steel absorber and covers a pseudorapidity range of $|\eta| < 2.5$. Next in η is the LAr Electromagnetic End-Cap (EMEC) that also uses lead-stainless steel absorber and the LAr Hadronic End-Cap (HEC) which has a copper plate absorber; both EMEC and HEC cover $1.5 < |\eta| < 3.2$. The final LAr calorimeter is the aptly named Forward Calorimeter (FCAL) that covers $|\eta| < 4.9$ and has three modules. The first is optimized for EM calorimetry and uses a copper absorber. The other two FCAL modules are used to measure hadronic showers and use tungsten absorbers.

The EMB and EMEC both utilize an accordion geometry pictured in Figure 3.14 to ensure a full ϕ coverage. The EMB consists of four layers, the first being a LAr presampler of 1.1 cm

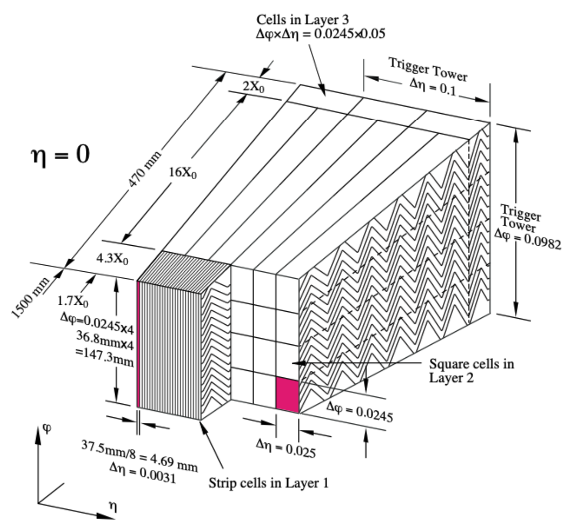

Figure 3.14: A EMB module showing the accordion geometry and granularity. [20]

thickness. The presampler is used to correct for energy losses due to material in front of the calorimeter. The first layer after the presampler is finely segmented to ensure good position measurements. The second layer is $16\,\chi_0$ thick and collects most of the electromagnetic showers. Typically, only the tails of EM showers make it to the third and final layer, so a courser granularity is used.

3.2.4.2 Tile Calorimeter

The hadronic Tile Calorimeter (TileCal) is a sampling calorimeter that is designed to fully absorb hadronic showers covering a range of $|\eta| < 1.7$ at a radial distance of

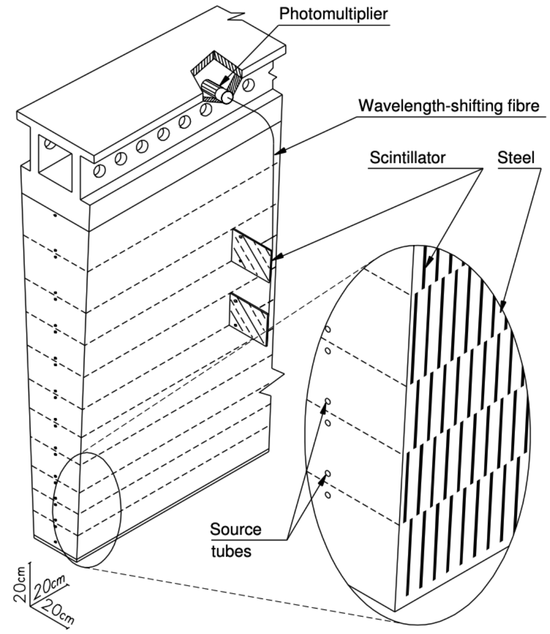

(a)

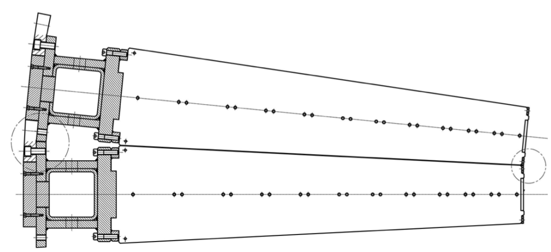

(b)

Figure 3.15: (a) Diagram of an individual TileCal module. (b) Azimuthal view of two TileCal modules with the IP being to the right.

$2.28\,\mathrm{m} \leq R \leq 4.25\,\mathrm{m}$ from the IP. This radial distance translates to approximately $7.4\,\lambda$. A similar design of absorber and electrode is used in TileCal to capture the full energy of hadronic showers. TileCal uses a steel absorber. However, instead of a liquid or gas being ionized and the free electrons being collected as a signal, TileCal takes advantage of a special material called scintillating plastic. When an ionizing particle interacts with the scintillating plastic, light is created; this light is absorbed in wavelength shifting (WLS) fibers. It is then re-emitted and transmitted to photomultiplier tubes (PMTs). The PMT signal is then shaped, amplified at two gains with a ratio of 64:1, then digitized at 40 MHz with 10-bit analogue-to-digital converters (ADCs). Each cell within TileCal has 2 PMTs, giving over 10,000 readout channels. There are 256 modules within TileCal. A diagram of an individual module and the layout of two modules side-by-side can be seen in Figure 3.15.

A significant fraction of the author's time and effort during their PhD went to data quality monitoring and maintenance of TileCal. These works are detailed in Appendix A.

3.2.5 Muon Spectrometer

High momentum muons provide a vital signature at the LHC. Muons are minimally ionizing particles, meaning they leave a small amount of energy inside detectors and travel to the edge and beyond the volume of the ATLAS detector. Instead of attempting to fully absorb muons, high precision position measurements are taken to track their trajectories. The toroid magnet system described in section 3.2.2.2 is an integral part of the Muon Spectrometer; it provides the bending force, changing the trajectories to the direction of the beamline. The barrel section of the Muon Spectrometer consists of three concentric cylindrical shells at $R = 5\,\mathrm{m}, 7.5\,\mathrm{m}, 10\,\mathrm{m}$ made of Monitored Drift Tubes (MDTs) ($|\eta| < 1$). [21] These cylindrical shells sit in-between and on the air core toroid magnets. On the 2$^{\mathrm{nd}}$ and 3$^{\mathrm{rd}}$ shells are Resistive Plate Chambers (RPCs) that provide quick triggering. Complimenting the barrel section are the end-caps, referred to as wheels for the Muon Spectrometer. The wheels are placed at $|z| \approx 7.4\,\mathrm{m}, 10.8\,\mathrm{m}, 14\,\mathrm{m}, \mathrm{and}\, 21.5\,\mathrm{m}$ $(2.0 < |\eta| < 2.7)$. The innermost layer of these wheels experience the highest rates of incident particles. To cope with this, Cathode Strip Chambers (CSCs) with a finer granularity than the MDTs that are used in the barrel. Similarly, Thin Gap Chambers (TGCs) are used for triggering instead of RPCs. These wheels provide spatial coordinates orthogonal to those of the precision-tracking MDTs in the barrel. Figure 3.16 shows the positioning of the various Muon Spectrometer components.[6]

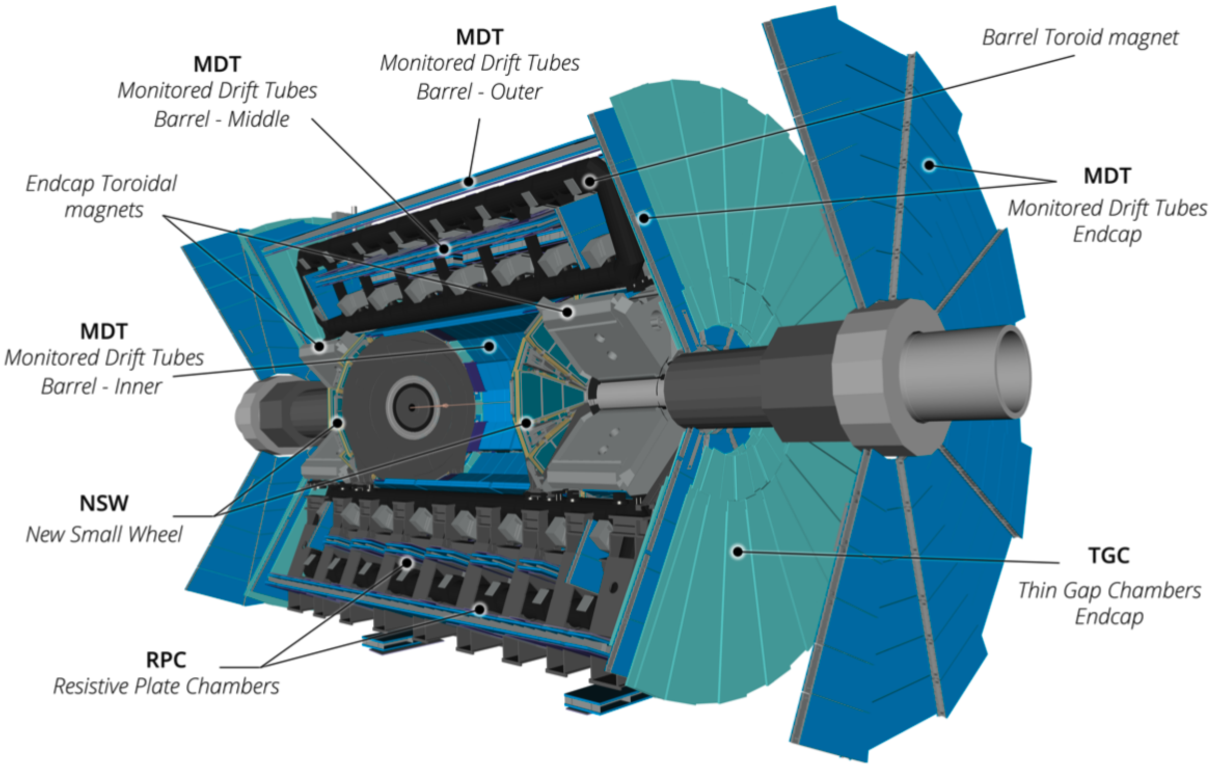

Figure 3.16: Cut-out view of the ATLAS detector Muon Spectrometer.

3.2.6 Trigger System

The high luminosity provided by the LHC is critical in collecting enough data to make detailed physics analyses. However, it also means that there is an incredibly large amount of data to sort through. So much that it is not possible to write out the data from every bunch crossing. As shown in Figure 3.6, even one single event can contain an inordinate amount

[6]Figure 3.16 Shows the New Small Wheel (NSW). The NSW is an upgrade to the old Small Wheels that were used in the data taking period that concerns this dissertation.

of data. Another issue arises due to the nature of hadron collisions; in that not all bunch crossing provide hard scatter inelastic collisions that are "interesting" enough to save data on.

To solve this issue, the data coming out of ATLAS is combed through in real time at a variable rate of 1 kHz to 40 MHz. This is done with a Trigger and Data Acquisition (TDAQ) system. The TDAQ system used in Run-2 is described in detail here: [22]. The TDAQ system reads in data from the ATLAS detector, calculates relevant quantities, and makes a decision on if there was an event worth storing. A diagram showing the data flow into the TDAQ system is show in 3.17.[7] The ATLAS TDAQ system consists of two main components, Level-1 (L1) and High Level Trigger (HLT). The L1 trigger is a hardware based trigger system that reads in data from the calorimeters and muon spectrometer. The L1 trigger has a latency of $2.5\,\mu$s and can read-out accepted events up to 100 kHz, the detector maximum readout rate. The HLT is a software based trigger system based on the offline reconstruction software. During Run-2 the HLT operated with an average output rate of 1.2 kHz, which translates to about 1.2 GB/s of data sent to permanent storage.

After the TDAQ system accepts an event, the data is set to be stored on magnetic tape for long term storage. It is also processed at the local computing farm named Tier-0 with the full reconstruction software suite described in Chapter 5.

[7] Figure 3.17 shows the Fast TracKer (FTK). During Run 2 FTK was undergoing commissioning and was not used in the active TDAQ system.

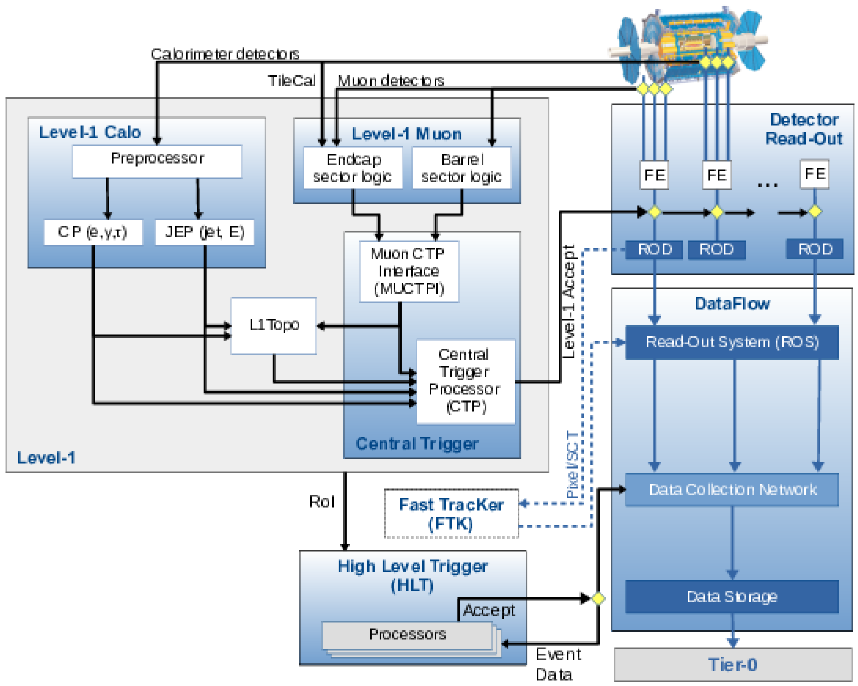

Figure 3.17: The ATLAS TDAQ system in Run-2 showing the components relevant for triggering as well as the detector read-out and data flow.

CHAPTER 4

SIMULATION

The data collected by the ATLAS experiment must be compared to a control. This control is most often a dataset of simulation particle collisions that approximate to great precision physics processes and particle interaction with detector material, as well as the detector's response. Figure 4.1 shows the chain of simulations these datasets are produced by.

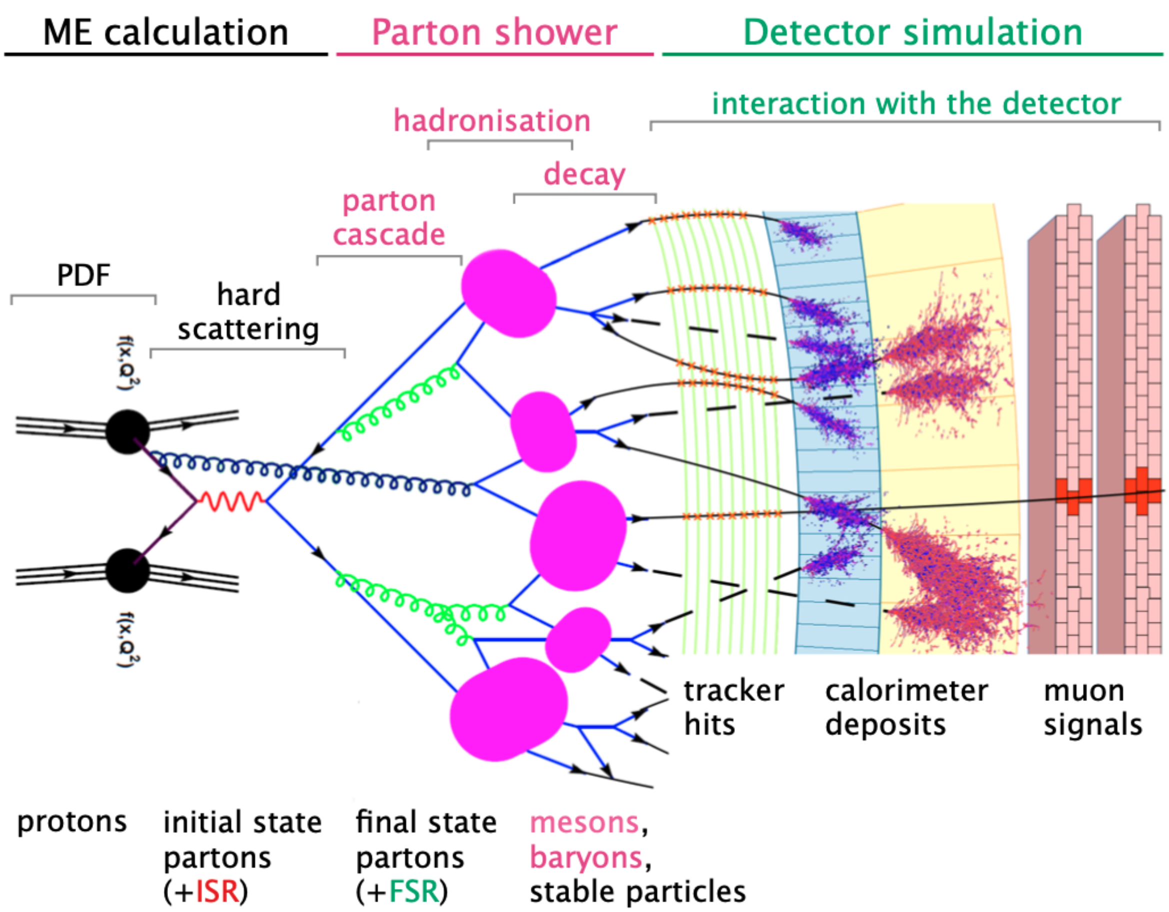

Figure 4.1: A pictorial representation of the simulation chain used in the ATLAS experiment. [23]

Many particle physics experiments, ATLAS included, use Monte Carlo (MC) simulation techniques to produce these datasets. Monte Carlo simulation techniques use repeated random sampling of underlying probability density functions to closely model various processes.

4.1 Event Generation and Hadronization

Since protons and other hadrons are not fundamental particles, it is impossible to know the exact constituents (partons) that interacted during a collision. To mimic this intrinsic probabilistic nature, Parton Distribution Functions (PDFs) are used. Where a PDF models the probability of any parton within a proton (or hadron) to carry a fraction of the beam energy as momentum. The PDF and subsequent inelastic hard scattering of the interacting partons are modeled via a Matrix Element (ME) calculation, often depicted through Feynman diagrams. This ME calculation is done to fixed order in perturbation theory, leading order (LO), next-to-leading order (NLO), leading-logarithmic order (LL), etc. This first level event generation can be done by a myriad of MC event generators. Often specific choices are made based on individual generator performance for a given physics process.

The next step in the simulation chain is the parton showering or hadronization. This is often done with a completely different set of MC generators. Hadronization is a complex, computationally expensive step to simulate and is done through iteratively. An example of a parton shower generator output can be seen in figure 4.2.

4.2 Detector Simulation

The final step in the simulation chain is simulating the particle's interaction with the detector material and the detector's response. Up until this point, the MC generators used are

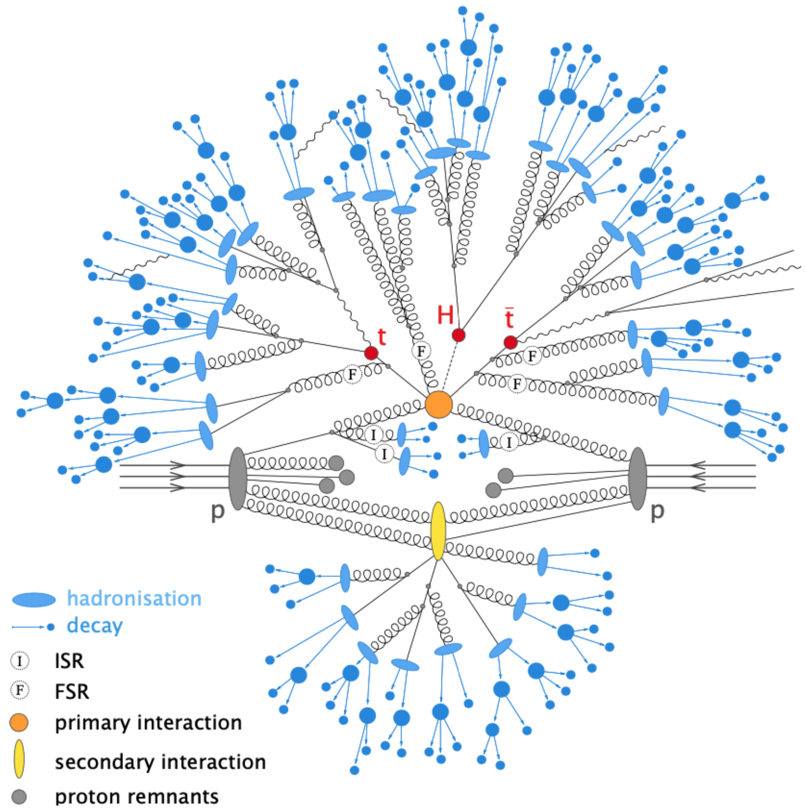

Figure 4.2: A pictorial representation of a parton shower of a ttH event. [23]

generic non-experiment dependent simulations. The ATLAS collaboration uses a GEANT4 based generator suite to simulate these interactions. [24] These simulations are incredibly detailed, including all support structure, material densities, readout electronics, digitization, etc. The final simulated dataset is output into a raw data format identical to real data coming off of the ATLAS detector.

CHAPTER 5

EVENT RECONSTRUCTION

5.1 Muon Identification

5.2 e γ Identification

5.3 Jet Clustering

5.3.1 b-jet Tagging

5.4 τ Identification

5.5 $E_{\mathbf{T}}^{\mathbf{miss}}$

CHAPTER 6

SEARCH FOR CHARGED HIGGS BOSONS

6.1 Signature and Event Selection

6.1.1 Object Definitions

6.1.2 Event Selections

6.2 Datasets

6.2.1 Signal Modeling

6.3 Background Modeling

6.4 Analysis Strategy

6.4.1 Multivariate Analysis Techniques

6.4.2 Training

6.4.3 Feature Selection

6.4.4 Hyperparameter Optimization

6.5 Systematic Uncertainties

6.6 Results

CHAPTER 7

CONCLUSION

Appendices

APPENDIX

TILECAL DATA QUALITY

BIBLIOGRAPHY

[1] R. L. Workman et al. “Review of Particle Physics”. *PTEP* 2022 (2022), p. 083C01. DOI: 10.1093/ptep/ptac097.

[2] P. W. Higgs. “Broken Symmetries and the Masses of Gauge Bosons”. *Phys. Rev. Lett.* 13 (16 Oct. 1964), pp. 508–509. DOI: 10.1103/PhysRevLett.13.508. URL: https://link.aps.org/doi/10.1103/PhysRevLett.13.508.

[3] F. Englert and R. Brout. “Broken Symmetry and the Mass of Gauge Vector Mesons”. *Phys. Rev. Lett.* 13 (9 Aug. 1964), pp. 321–323. DOI: 10.1103/PhysRevLett.13.321. URL: https://link.aps.org/doi/10.1103/PhysRevLett.13.321.

[4] J. Ellis. “Higgs Physics” (Dec. 2013). 52 pages, 45 figures, Lectures presented at the ESHEP 2013 School of High-Energy Physics, to appear as part of the proceedings in a CERN Yellow Report, 117–168. 52 p. DOI: 10.5170/CERN-2015-004.117. arXiv: 1312.5672. URL: https://cds.cern.ch/record/1638469.

[5] G. A. et al. “Observation of a new particle in the search for the Standard Model Higgs boson with the ATLAS detector at the LHC”. *Physics Letters B* 716.1 (2012), pp. 1–29.

[6] G. Branco et al. “Theory and phenomenology of two-Higgs-doublet models”. *Physics Reports* 516.1–2 (July 2012), pp. 1–102. ISSN: 0370-1573. DOI: 10.1016/j.physrep.2012.02.002. URL: http://dx.doi.org/10.1016/j.physrep.2012.02.002.

[7] J. R. Andersen et al. “Handbook of LHC Higgs Cross Sections: 3. Higgs Properties” (2013). Ed. by S. Heinemeyer et al. DOI: 10.5170/CERN-2013-004. arXiv: 1307.1347 [hep-ph].

[8] M. Aaboud et al. “Search for charged Higgs bosons decaying via $H^{\pm} \rightarrow \tau^{\pm}\nu_{\tau}$ in the τ+jets and τ+lepton final states with 36 fb^{-1} of pp collision data recorded at $\sqrt{s} = 13$

TeV with the ATLAS experiment”. *JHEP* 09 (2018), p. 139.
DOI: 10.1007/JHEP09(2018)139. arXiv: 1807.07915 [hep-ex].

[9] CERN. *Facts and figures about the LHC*.
URL: https://home.cern/resources/faqs/facts-and-figures-about-lhc.

[10] L. R. Evans and P. Bryant. “LHC Machine”. *JINST* 3 (2008). This report is an abridged version of the LHC Design Report (CERN-2004-003), S08001. 164 p.
DOI: 10.1088/1748-0221/3/08/S08001.
URL: https://cds.cern.ch/record/1129806.

[11] X. C. Vidal and R. C. Manzano. *Lorentz Force Taking a closer look at LHC*. URL: https://www.lhc-closer.es/taking_a_closer_look_at_lhc/0.lorentz_force.

[12] E. Lopienska. “The CERN accelerator complex, layout in 2022. Complexe des accélérateurs du CERN en janvier 2022” (Feb. 2022). General Photo.
URL: https://cds.cern.ch/record/2800984.

[13] *Pseudorapidity*. Wikipedia, Feb. 2009.
URL: https://en.wikipedia.org/wiki/File:Pseudorapidity2.png.

[14] *ATLAS central solenoid: Technical Design Report*. Technical design report. ATLAS. Electronic version not available. Geneva: CERN, 1997.
DOI: 10.17181/CERN.ZZVJ.2JYE. URL: https://cds.cern.ch/record/331067.

[15] *ATLAS tile calorimeter: Technical Design Report*. Technical design report. ATLAS. Geneva: CERN, 1996. DOI: 10.17181/CERN.JRBJ.7O28.
URL: https://cds.cern.ch/record/331062.

[16] J. P. Badiou et al. *ATLAS barrel toroid: Technical Design Report*.
Technical design report. ATLAS. Electronic version not available.

Geneva: CERN, 1997. DOI: 10.17181/CERN.RF2A.CP5T.
URL: https://cds.cern.ch/record/331065.

[17] N. Wermes and G. Hallewel. *ATLAS pixel detector: Technical Design Report*. Technical design report. ATLAS. Geneva: CERN, 1998. URL: https://cds.cern.ch/record/381263.

[18] M. Capeans et al. *ATLAS Insertable B-Layer Technical Design Report*. Tech. rep. Sept. 2010. URL: https://cds.cern.ch/record/1291633.

[19] *ATLAS inner detector: Technical Design Report, 1*. Technical design report. ATLAS. Geneva: CERN, 1997. URL: https://cds.cern.ch/record/331063.

[20] The ATLAS Collaboration. "The ATLAS Experiment at the CERN Large Hadron Collider". *Journal of Instrumentation* 3.08 (Aug. 2008), S08003–S08003. DOI: 10.1088/1748-0221/3/08/s08003. URL: https://doi.org/10.10882F1748-02212F32F082Fs08003.

[21] *ATLAS muon spectrometer: Technical Design Report*. Technical design report. ATLAS. Geneva: CERN, 1997. URL: https://cds.cern.ch/record/331068.

[22] T. A. collaboration. "Operation of the ATLAS trigger system in Run 2". *Journal of Instrumentation* 15.10 (Oct. 2020), P10004–P10004. DOI: 10.1088/1748-0221/15/10/p10004. URL: https://doi.org/10.1088/1748-0221/15/10/p10004.

[23] C. Wanotayaroj. "Search for a Scalar Partner of the Top Quark in the Jets+MET Final State with the ATLAS detector". Presented 25 Oct 2016. Nov. 2016. URL: http://cds.cern.ch/record/2242196.

[24] S. Agostinelli et al. “Geant4—a simulation toolkit”. *Nuclear Instruments and Methods in Physics Research Section A: Accelerators, Spectrometers, Detectors and Associated Equipment* 506.3 (2003), pp. 250–303. ISSN: 0168-9002. DOI: https://doi.org/10.1016/S0168-9002(03)01368-8. URL: https://www.sciencedirect.com/science/article/pii/S0168900203013688.